

International Journal of Modern E  
© World Scientific Publishing Company

**DESCRIPTION OF DRIP-LINE NUCLEI  
WITHIN RELATIVISTIC MEAN FIELD PLUS BCS APPROACH**

H. L. Yadav<sup>1,2\*</sup>, M. Kaushik<sup>1</sup>, H. Toki<sup>2,3,†</sup>

<sup>1</sup> *Department of Physics, Rajasthan University, Jaipur 302004, India*

<sup>2</sup> *Research Center for Nuclear Physics (RCNP), Osaka University, 10-1, Mihogaoka  
Ibaraki, Osaka 567-0047, Japan*

<sup>3</sup> *The Institute of Physical and Chemical Research (RIKEN), 2-1 Hirosawa  
Wako, Saitama 351-0198, Japan*

Received (received date)

Revised (revised date)

\*email: hlyadav@sancharnet.in (H. L. Yadav)

†email: toki@rcnp.osaka-u.ac.jp (H. Toki)

Recently it has been demonstrated, considering Ni and Ca isotopes as prototypes, that the relativistic mean-field plus BCS (RMF+BCS) approach wherein the single particle continuum corresponding to the RMF is replaced by a set of discrete positive energy states for the calculation of pairing energy provides a good approximation to the full relativistic Hartree-Bogoliubov (RHB) description of the ground state properties of the drip-line neutron rich nuclei. The applicability of RMF+BCS approach even for the drip-line nuclei is essentially due to the fact that the main contribution to the pairing correlations for the neutron rich nuclei is provided by the low-lying resonant states, in addition to the contributions coming from the states close to the Fermi surface. In order to show the general validity of this approach we present here the results of our detailed calculations for the ground state properties of the chains of isotopes of O, Ca, Ni, Zr, Sn and Pb nuclei. The TMA force parameter set has been used for the effective mean-field Lagrangian with the nonlinear terms for the sigma and omega mesons. Further, to check the validity of our treatment for different mean-field descriptions, calculations have also been carried out for the NL-SH force parameterization usually employed for the description of drip-line nuclei. Comprehensive results for the two neutron separation energy, rms radii, single particle pairing gaps and pairing energies etc. are presented. Especially, the Ca isotopes are found to exhibit distinct features near the neutron drip line whereby it is found that further addition of neutrons causes a rapid increase in the neutron rms radius with almost no increase in the binding energy, indicating the occurrence of halos. It is mainly caused by the pairing correlations and results in the existence of bound states of extremely neutron rich exotic nuclei. Similar characteristics though less pronounced, are also exhibited by the neutron rich Zr isotopes. A comparison of these results with the available experimental data and with the recent continuum relativistic Hartree-Bogoliubov (RCHB) calculations amply demonstrates the validity and usefulness of this fast RMF+BCS approach for the description of nuclei including those near the drip-lines.

*Keywords:* Drip-line nuclei; Relativistic mean-field plus BCS approach; Comparison with RCHB; Two neutron separation energy; Neutron and proton density distributions, radii; Halo formation; Chains of isotopes of O, Ca, Ni, Zr, Sn and Pb nuclei. PACS:21.10.-k, 21.10.Ft, 21.10.Dr, 21.10.Gv, 21.60.-n, 21.60.Jz, 22.50.+e

## 1. Introduction

Production of radioactive beams have facilitated the nuclear structure studies away from the line of  $\beta$ -stability, especially for the neutron rich nuclei. The structure of these exotic nuclei with unusually large  $|N - Z|$  value is characterized by several interesting features. It exhibits extremely small separation energy of the outermost nucleons and the Fermi level lies close to the single particle continuum. In the case of neutron drip-line nuclei the neutron density distribution shows a much extended tail with a diffused neutron skin<sup>1</sup>. In some cases it even leads to the phenomenon of neutron halo made of several neutrons outside a core with separation energy of the order of 100 keV or less. Due to the weak binding and large spatial dimension of the outermost nucleons, the role of continuum states and their coupling to the bound states become exceedingly important, especially for the pairing energy contribution to the total binding energy of the system. Theoretical investigations of such nuclei have been carried out extensively within the framework of mean field theories such as Hartree-Fock-Bogoliubov (HFB), HF+BCS<sup>2-7</sup> and their relativistic counterparts<sup>8-22</sup>. A detailed comparative study of the HFB approach with those

of the HFB based on the box boundary conditions, and the HF+BCS+Resonant continuum approach has been carried out by Grasso *et al.*<sup>7</sup> providing insight to the validity of different approaches for the treatment of drip-line nuclei. Earlier Sandulescu *et al.*<sup>6</sup> have also studied the effect of resonant continuum on the properties of neutron rich nuclei within the HF+BCS approximation. The interesting result of these investigation is that only a few low energy resonant states, especially those near the Fermi surface influence in an appreciable way the pairing properties of nuclei far from the  $\beta$ -stability. Indeed, comparison between the results given by the resonant continuum HF+BCS<sup>6</sup> and the continuum HFB calculations<sup>7</sup> shows that a few low-lying resonances give practically the full effect of the continuum on pairing related properties. This finding has proved to be of immense significance because one can eventually make systematic studies of a large number of nuclei by using a simpler HF+BCS approximation.

Recently the relativistic mean field (RMF) theory has been extensively used for the study of unstable nuclei<sup>14,16,17</sup>. The advantage of the RMF approach is that it provides the spin-orbit interaction in the entire mass region, which is consistent with the nucleon density<sup>8,10</sup>. This indeed could be very important for the study of unstable nuclei near the drip line, since the single particle properties near the threshold change largely as compared to the case of deeply bound levels in the nuclear potential. In addition to this, the pairing properties are also important for nuclei near the drip line where we have to take into account the coupling of bound pairs with the pairs in the continuum. In order to take into account the pairing correlations together with a realistic mean field, the framework of RHB approach is commonly used<sup>19,20</sup>. In this connection, the finding above for the non-relativistic frameworks has turned out to be very important for the systematic work of unstable nuclei in the relativistic approach. This has been demonstrated recently by Yadav *et al.*<sup>28</sup> for the case of <sup>48–98</sup>Ni isotopes. Indeed the RMF+BCS scheme<sup>28</sup> wherein the single particle continuum corresponding to the RMF is replaced by a set of discrete positive energy states yields results which are found to be in close agreement with the experimental data and with those of recent continuum relativistic Hartree-Bogoliubov (RCHB) and other similar mean-field calculations<sup>19,26</sup>. In fact the applicability of RMF+BCS approach even for the drip-line nuclei is essentially due to the fact that the main contribution to the pairing correlations for the neutron rich nuclei is provided by the low-lying resonant states, in addition to the contributions coming from the states close to the Fermi surface.

With the success of the RMF+BCS approach for the prototype calculations of Ni and Ca isotopes<sup>28</sup>, it is natural to investigate its validity for other nuclei in different regions of the periodic table. Also it would be interesting to check the results with different popular RMF force parameterizations. With this in view we have carried out detailed calculations for the chains of isotopes of O, Ca, Zr, Sn and Pb nuclei using the TMA and the NLSH force parameterizations. Excepting Zr, the other nuclei considered in this studies are proton magic nuclei. The results of these calculations for the two neutron separation energy, neutron, proton, and matter rms radii, and single particle pairing gaps etc., and their comparison with the available experimental data and with the RCHB results are presented here to demonstrate the general validity of our RMF+BCS approach.

## 2. Theoretical Formulation and Model

Our RMF calculations have been carried out using the model Lagrangian density with nonlinear terms both for the  $\sigma$  and  $\omega$  mesons as described in detail in Ref. <sup>17</sup>, which is given by

$$\begin{aligned}
 \mathcal{L} = & \bar{\psi}[\not{v}\gamma^\mu\partial_\mu - M]\psi \\
 & + \frac{1}{2}\partial_\mu\sigma\partial^\mu\sigma - \frac{1}{2}m_\sigma^2\sigma^2 - \frac{1}{3}g_2\sigma^3 - \frac{1}{4}g_3\sigma^4 - g_\sigma\bar{\psi}\sigma\psi \\
 & - \frac{1}{4}H_{\mu\nu}H^{\mu\nu} + \frac{1}{2}m_\omega^2\omega_\mu\omega^\mu + \frac{1}{4}c_3(\omega_\mu\omega^\mu)^2 - g_\omega\bar{\psi}\gamma^\mu\psi\omega_\mu \\
 & - \frac{1}{4}G_{\mu\nu}^a G^{a\mu\nu} + \frac{1}{2}m_\rho^2\rho_\mu^a\rho^{a\mu} - g_\rho\bar{\psi}\gamma_\mu\tau^a\psi\rho^{\mu a} \\
 & - \frac{1}{4}F_{\mu\nu}F^{\mu\nu} - e\bar{\psi}\gamma_\mu\frac{(1-\tau_3)}{2}A^\mu\psi, \tag{1}
 \end{aligned}$$

where the field tensors  $H$ ,  $G$  and  $F$  for the vector fields are defined by

$$\begin{aligned}
 H_{\mu\nu} &= \partial_\mu\omega_\nu - \partial_\nu\omega_\mu \\
 G_{\mu\nu}^a &= \partial_\mu\rho_\nu^a - \partial_\nu\rho_\mu^a - 2g_\rho\epsilon^{abc}\rho_\mu^b\rho_\nu^c \\
 F_{\mu\nu} &= \partial_\mu A_\nu - \partial_\nu A_\mu,
 \end{aligned}$$

and other symbols have their usual meaning.

The set of parameters appearing in the effective Lagrangian (1) have been obtained in an extensive study which provides a good description for the ground state of nuclei and that of the nuclear matter properties<sup>17</sup>. This set, termed as TMA, has an  $A$ -dependence and covers the light as well as heavy nuclei from <sup>16</sup>O to <sup>208</sup>Pb. Table 1 lists the TMA set of parameters along with the results for the calculated bulk properties of nuclear matter. As mentioned earlier we have also carried the RMF+BCS calculations using the NL-SH force parameters<sup>27</sup> in order to compare our results with those obtained in the RHB calculations<sup>26</sup> using this force parameterization. The NL-SH parameters are also listed in Table 1 together with the corresponding nuclear matter properties.

Based on the single-particle spectrum calculated by the RMF described above, we perform a state dependent BCS calculations<sup>23,24</sup>. As we already mentioned, the continuum is replaced by a set of positive energy states generated by enclosing the nucleus in a spherical box. Thus the gap equations have the standard form for all the single particle states, i.e.

$$\Delta_{j_1} = -\frac{1}{2}\frac{1}{\sqrt{2j_1+1}}\sum_{j_2}\frac{\langle(j_1^2)0^+|V|(j_2^2)0^+\rangle}{\sqrt{(\varepsilon_{j_2}-\lambda)^2+\Delta_{j_2}^2}}\sqrt{2j_2+1}\Delta_{j_2}, \tag{2}$$

where  $\varepsilon_{j_2}$  are the single particle energies, and  $\lambda$  is the Fermi energy, whereas the particle number condition is given by  $\sum_j(2j+1)v_j^2 = N$ . In the calculations we use for the pairing interaction a delta force, i.e.,  $V = -V_0\delta(r)$  with the same strength  $V_0$  for both protons and neutrons. The value of the interaction strength  $V_0 = 350 \text{ MeV fm}^3$  was determined by obtaining a best fit to the binding energy of

Ni isotopes. We use the same value of  $V_0 = 350$  for our present studies of isotopes of other nuclei as well. Apart from its simplicity, the applicability and justification of using such a  $\delta$ -function form of interaction has been recently discussed in Refs. 2 and 4, whereby it has been shown in the context of HFB calculations that the use of a delta force in a finite space simulates the effect of finite range interaction in a phenomenological manner. The pairing matrix element for the  $\delta$ -function force is given by

$$\langle (j_1^2) 0^+ | V | (j_2^2) 0^+ \rangle = -\frac{V_0}{8\pi} \sqrt{(2j_1+1)(2j_2+1)} I_R, \quad (3)$$

where  $I_R$  is the radial integral having the form

$$I_R = \int dr \frac{1}{r^2} (G_{j_1}^* G_{j_2} + F_{j_1}^* F_{j_2})^2 \quad (4)$$

Here  $G_\alpha$  and  $F_\alpha$  denote the radial wave functions for the upper and lower components, respectively, of the nucleon wave function expressed as

$$\psi_\alpha = \frac{1}{r} \begin{pmatrix} i G_\alpha \mathcal{Y}_{j_\alpha l_\alpha m_\alpha} \\ F_\alpha \sigma \cdot \hat{r} \mathcal{Y}_{j_\alpha l_\alpha m_\alpha} \end{pmatrix}, \quad (5)$$

and satisfy the normalization condition

$$\int dr \{|G_\alpha|^2 + |F_\alpha|^2\} = 1 \quad (6)$$

In Eq. (5) the symbol  $\mathcal{Y}_{jlm}$  has been used for the standard spinor spherical harmonics with the phase  $i^l$ . The coupled field equations obtained from the Lagrangian density in (1) are finally reduced to a set of simple radial equations<sup>10</sup> which are solved self consistently along with the equations for the state dependent pairing gap  $\Delta_j$  and the total particle number  $N$  for a given nucleus.

### 3. Results and Discussion

The present RMF+BCS calculations are restricted to the spherical shape and have been carried out for the entire chain of isotopes of proton magic nuclei O, Ca, Ni, Sn and Pb as well as those of isotopes of Zr with proton sub-magic number  $Z=40$ . We note that earlier non-relativistic as well as relativistic calculations indicate that Zr nuclei with  $A > 122$  are spherical<sup>29</sup>. It is found that the isotopes of Ca and Zr, to a large extent, exhibit similar characteristics near the drip line which is pushed out to unusually heavy neutron rich isotopes. Similarly the isotopes of Ni, Sn, Pb and that of O yield results with common features. Thus in order to save space, we have made the presentation of results in the following manner. First a detailed description of the Ca and Ni isotopes is given as representative cases of the nuclei considered in the present investigation. This is then followed by a description of the results for the rest of the nuclei O, Zr, Sn and Pb.

Again, from amongst the chain of isotopes of these nuclei, we consider only a few of the selected neutron rich isotopes to describe in detail their single particle spectra

and resonant states, and their pairing gap energies etc. These chosen isotopes are considered here as representative cases in order to demonstrate the main properties of neutron rich isotopes for a particular element. The total pairing energy contribution to the binding energy of the system plays a crucial role in the understanding of exotic nuclei and has been described next. This is followed by a detailed description of the results of two neutron separation energies, proton and neutron radii, and the density distributions for the chains of isotopes of different nuclei mentioned above.

Furthermore, the structure of single particle spectra near the Fermi level, and its variation with further addition of neutrons have been usefully employed to explain the results for the two-neutron drip line, and also for the possibility of occurrence of neutron halos as well as for the asymptotic radial dependence of the neutron density distributions. These involve both the bound as well as positive energy states in the continuum. These states play an important role as scattering of particles from bound to continuum states near the Fermi level and vice versa due to the pairing interaction involves mainly these very states. The last few occupied states near the Fermi level also provide an understanding of the radii of the loosely bound exotic nuclei. The neutron rich nuclei in which the last filled single particle state near the Fermi level is of low angular momentum ( $s_{1/2}$  or  $p_{1/2}$  state), especially the  $l = 0$  state, can have large radii due to large spatial extension of the  $s_{1/2}$  state which has no centrifugal barrier. In our calculations such a situation is seen to occur in the neutron rich Ca isotopes wherein the last single particle state involved is the  $3s_{1/2}$  leading to halo like phenomenon already well known in light nuclei. Similar effect, though less pronounced, is found in the neutron rich Zr isotope due to the  $3p_{1/2}$  and  $3sp_{3/2}$  states near the Fermi level. In contrast, the single particle structures in the neutron rich Ni, Sn and Pb isotopes do not favor the formation of such halos as has been described later.

As stated earlier our RMF+BCS calculations have been performed with two different force parameterizations, TMA and NL-SH, in order to check if the results have any dependence on different mean field descriptions. Details of our calculations show that the two interactions employed here produce very similar results and, therefore, for the detailed description of single particle and resonant states mentioned above, we have presented results obtained with only the TMA force.

### **3.1. Ca Isotopes**

Neutron rich members of Ca isotopes constitute interesting example of loosely bound system. In order to describe the contribution of various single particle states to the pairing energy, we plot in fig. 1 the calculated RMF potential, a sum of scalar and vector potentials, for the neutron rich nucleus  $^{62}\text{Ca}$  along with the spectrum for the bound neutron single particle states. This is a typical example of the neutron rich nucleus amongst the Ca isotopes. The figure also shows the positive energy state corresponding to the first low-lying resonance  $1g_{9/2}$ , and other positive energy states, for example,  $3s_{1/2}$ ,  $2d_{5/2}$ ,  $2d_{3/2}$  and  $1g_{7/2}$  close to the Fermi surface which play significant role for the binding of neutron rich isotopes, ranging from  $^{62}\text{Ca}$  to  $^{72}\text{Ca}$ , through their contributions to the total pairing energy. In contrast to other states in the box which correspond to the non-resonant continuum, the position of the resonant  $1g_{9/2}$  state is not much affected by changing the box radius around

$R = 30$  fm. For the purpose of illustration we have also depicted in fig. 1 the total mean field potential for the neutron  $1g_{9/2}$  state, obtained by adding the centrifugal potential energy.

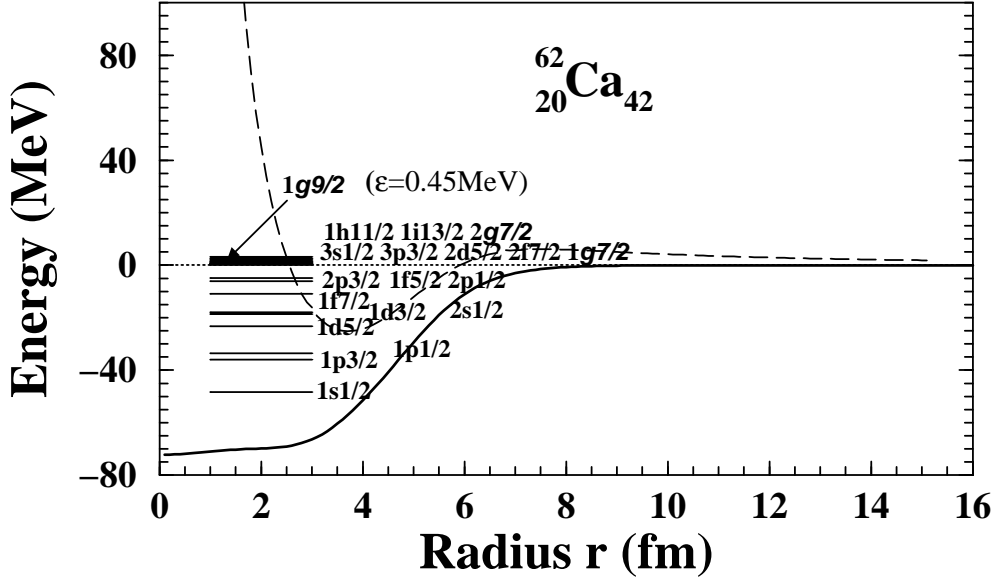


**Fig. 1.** The RMF potential energy (sum of the scalar and vector potentials), for the nucleus  $^{62}\text{Ca}$  as a function of radius is shown by the solid line. The long dashed line represents the sum of RMF potential energy and the centrifugal barrier energy for the neutron resonant state  $1g_{9/2}$ . The figure also shows the energy spectrum of some important neutron single particle states along with the resonant  $1g_{9/2}$  state at 0.45 MeV. A few high lying continuum states like  $1h_{11/2}$ ,  $1i_{13/2}$  etc. are also indicated.

It is evident from the figure that the effective total potential for the  $1g_{9/2}$  state has an appreciable barrier for the trapping of waves to form a quasi-bound or resonant state. Such a meta-stable state remains mainly confined to the region of the potential well and the wave function exhibits characteristics similar to that of a bound state. This is clearly observed in fig. 2 which depicts the radial wave functions of some of the neutron single particle states lying close to the Fermi surface, the neutron Fermi energy being  $\lambda_n = -0.204$  MeV. These include the bound  $1f_{5/2}$  and  $2p_{1/2}$ , and the continuum  $3s_{1/2}$  and  $2d_{5/2}$  states in addition to the state corresponding to the resonant  $1g_{9/2}$ .

The wave function for the  $1g_{9/2}$  state plotted in fig. 2 is clearly seen to be confined within a radial range of about 8 fm and has a decaying component outside this region, characterizing a resonant state. In contrast, the main part of the wave function for the non-resonant states, e.g.  $2d_{5/2}$ , is seen to be spread over outside the potential region, though a small part is also contained inside the potential range. This type of state thus has a poorer overlap with the bound states near the Fermi surface leading to small value for the pairing gap  $\Delta_{2d_{5/2}}$ . Further, the positive

energy states lying much higher from the Fermi level, for example,  $1h_{11/2}$ ,  $1i_{13/2}$  etc. have a negligible contribution to the total pairing energy of the system.

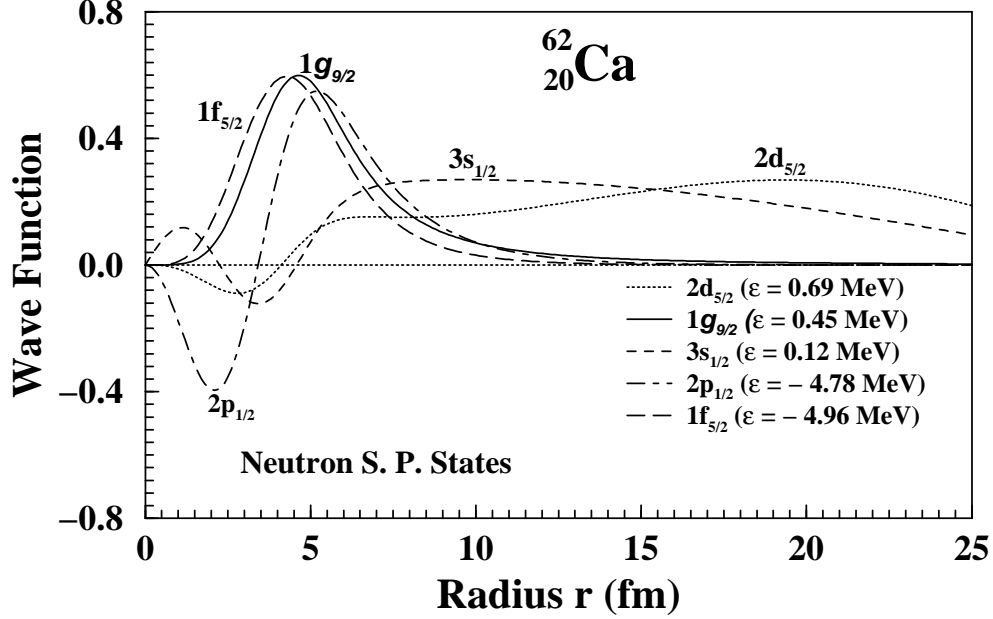


**Fig. 2.** Radial wave functions of a few representative neutron single particle states with energy close to the Fermi surface for the nucleus  $^{62}\text{Ca}$ . The solid line shows the resonant  $1g_{9/2}$  state at energy 0.45 MeV, while the bound  $1f_{5/2}$  state at -4.96 MeV, and  $2p_{1/2}$  state at -4.78 MeV are shown by long dashed line, and dashed -dotted lines, respectively. The  $3s_{1/2}$  and  $2d_{5/2}$  states with positive energies 0.12 MeV and 0.69 MeV have been depicted by small dashed and dotted lines, respectively.

These features can be seen from fig. 3 which depicts the calculated pairing gap energy  $\Delta_j$  for the neutron states in the nucleus  $^{62}\text{Ca}$ . However, we have not shown in the figure the single particle states having very small  $\Delta_j$  values as these do not contribute significantly to the total pairing energy. One observes indeed in fig. 3 that the gap energy for the  $1g_{9/2}$  state has a value close to 1 MeV which is quantitatively similar to that of bound states  $1f_{7/2}$  and  $2p_{3/2}$  etc. Also, fig. 3 shows that the pairing gap values for the non-resonant states like  $3s_{1/2}$  and  $2d_{5/2}$  in continuum have much smaller gap energy. However, as the number of neutrons increases while approaching the neutron drip line nucleus  $^{72}\text{Ca}$ , the single particle states  $3s_{1/2}$ ,  $1g_{9/2}$ ,  $2d_{5/2}$  and  $2d_{3/2}$  which lie near the Fermi level gradually come down close to zero energy, and subsequently the  $1g_{9/2}$  and  $3s_{1/2}$  states even become bound states. This helps in accommodating more and more neutrons which are just bound. In fact, the occupancy of the  $3s_{1/2}$  state in these extremely neutron rich isotopes causes the halo formation as will be discussed later.



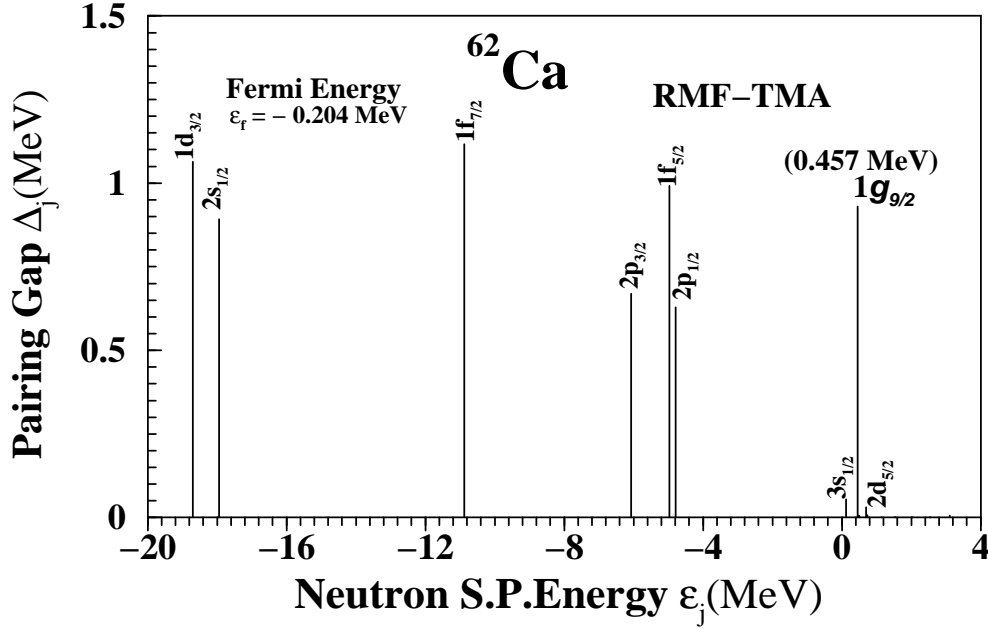


**Fig. 3.** Pairing gap energy  $\Delta_j$  of neutron single particle states with energy close to the Fermi surface for the nucleus  $^{62}\text{Ca}$ . The resonant  $1g_{9/2}$  state at energy 0.457 MeV has the gap energy of about 1 MeV which is close to that of bound states like  $1f_{5/2}$ ,  $1f_{7/2}$ ,  $1d_{3/2}$  etc.

The contribution of pairing energy plays an important role for the stability of the neutron rich nuclei and consequently in deciding the position of the neutron and proton drip lines. It is noted again that the RMF+BCS calculations carried out with two different sets of force parameters, the TMA and NL-SH, yield almost similar results also for the pairing energies for the isotopes of various nuclei considered in the present investigation. In fig. 4. this has been shown for the case of Ca isotopes. The differences in the two results can be attributed to the difference in the detailed structure of single particle energies obtained with the TMA and NL-SH forces. It is seen from fig. 4 that the pairing energy vanishes for the neutron numbers  $N = 14, 20, 28$  and  $40$  indicating the shell closures. It is observed that the usual shell closure at  $N = 50$  is absent for the neutron rich Ca isotopes and at  $N = 40$  a new shell closure appears. Also, for  $N = 52$  the pairing energy value is rather small. This reorganization of single particle energies with large values of  $N/Z$  ratio (for the neutron rich Ca isotopes  $N/Z \geq 2$ ) has its origin in the deviation of the strength of spin-orbit splitting from the conventional shell model results for nuclei with not so large  $N/Z$  ratio. Further, from the figure one sees the appearance of a new shell closure at the neutron number  $N = 14$ . This represents the case of nuclei having large number of protons as compared to that of neutrons.

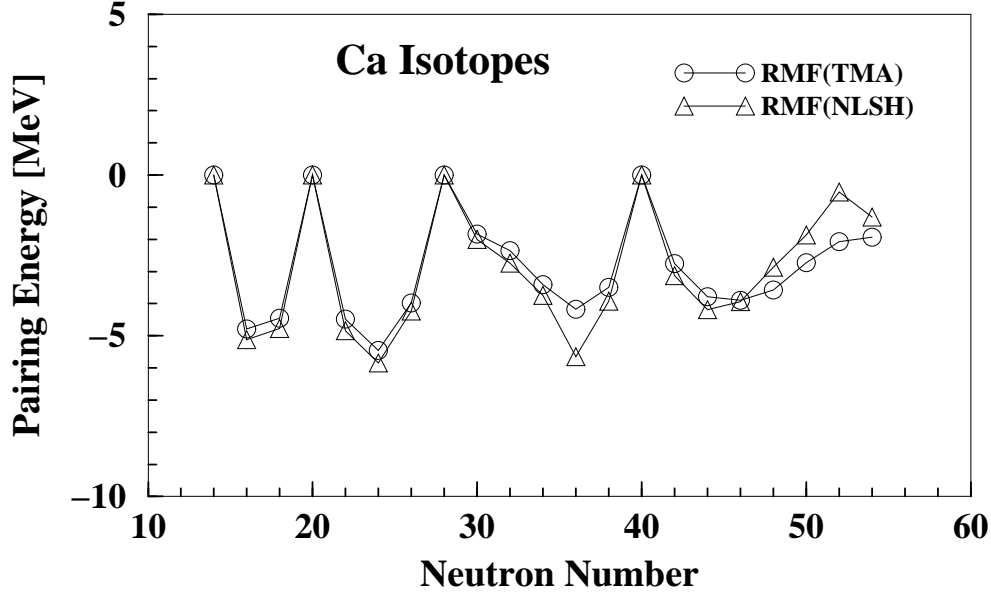
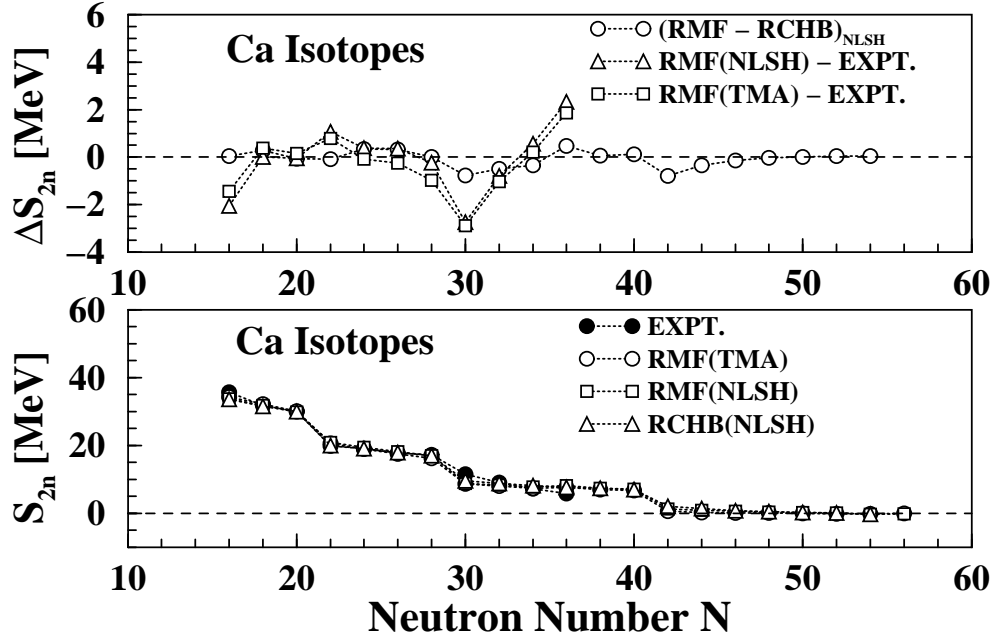


Fig. 4. Present RMF results for the pairing energy for the Ca isotopes obtained with the TMA (open circles) are compared with those obtained using the NL-SH (open triangles) force parameters.

It is also seen from the figure that the pairing energies for the nuclei falling in between two closed shells, as expected, increases from zero and have maximum values in the middle of the two closed shells. For the neutron rich Ca isotopes there is a tendency of slow rate of change in the pairing energy while one moves from one isotope to another. The shell structure as revealed by the pairing energies are also exhibited in the variation of two neutron separation energies  $S_{2n}$  as shown in fig. 5 for the Ca isotopes. An abrupt increase in the  $S_{2n}$  values for the isotopes next to magic numbers is evidently seen in Fig. 5. Thus, appearance of new magic numbers as well as the disappearance of conventional magic numbers for nuclei with extreme isospin values are expected to be quite general feature related to the reorganization of the single particle states due to changed characteristics of the spin-orbit splitting heather to known from stable nuclei with normal isospin values.

The two neutron separation energies provide a crucial means to check the validity of model calculations as extensive experimental data are available for long chains of isotopes of the nuclei considered in the present investigation. It is important to emphasize that such extensive experimental data are not available for the rms radii and charge densities especially for the neutron rich isotopes. In the lower panel of Fig. 5 we present the results of two neutron separation energy and their comparison with the RCHB, and also with available experimental data, for the even-even  $^{34-76}\text{Ca}$  isotopes. As stated earlier, in order to check the validity of our treatment for different mean field descriptions, calculations have been done

for two different RMF parameterizations: the TMA<sup>17</sup> force discussed above and the NL-SH<sup>27</sup> force often used for the drip-line nuclei. The upper panel of fig. 5 depicts the difference between the experimental and calculated values as well as the difference between our RMF+BCS predictions and those obtained from the RCHB approach<sup>26</sup>.



**Fig. 5.** Lower panel: The present RMF results for the two neutron separation energy for the Ca isotopes obtained with the TMA (open circles) and the NL-SH (open squares) force parameters are compared with the continuum relativistic Hartree-Bogoliubov (RCHB) calculations of Ref. 26 carried out with the NL-SH force (open triangles). The two neutron drip line is predicted to occur at  $N = 52$  corresponding to  $^{72}\text{Ca}$ . This part of the plot also depicts the available experimental data<sup>25</sup> (solid circles) for the purpose of comparison. Upper panel: It depicts the difference in the RMF+BCS results and the RCHB results of Ref. 26 for the two neutron separation energy obtained for the NL-SH force. the plot also shows the difference of the calculated results with respect to the available experimental data<sup>25</sup>.

The interesting results for the Ca isotopes is that the isotopes beyond  $A=66$  have two neutron separation energy close to zero. It is seen from the figure that the two forces yield similar results. The small differences, especially for the isotopes with  $N > 42$ , are due to difference in the energy spacing between the neutron  $1g_{9/2}$ , and the neutron  $3s_{1/2}$  and  $2d_{5/2}$  single particle states in the two RMF descriptions. Our calculations for the TMA description predicts that the heaviest stable isotope against two neutron emission corresponds to  $A=70$  ( $N=50$ ) whereas for the the NL-

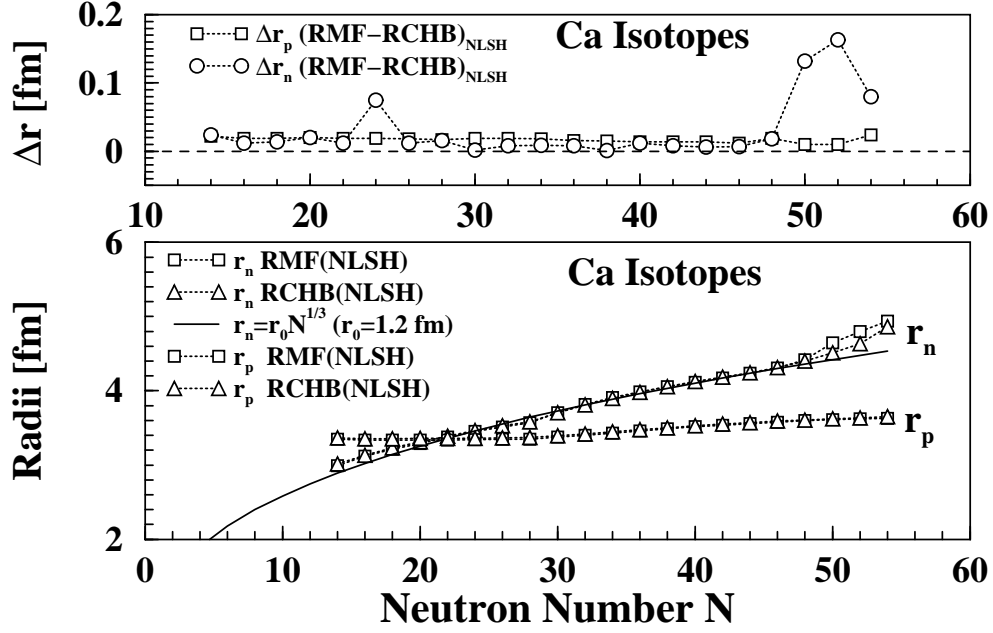
SH force it corresponds to  $A=72$  ( $N=52$ ). As mentioned above, since the isotopes beyond  $A=66$  are just bound this difference in the two mean-field description is not of much significance and should not be taken too seriously. The isotopes with mass number  $70 < A < 76$  for the TMA, and those with  $72 < A < 76$  for the NL-SH case are similarly found to be just unbound with negative separation energy very close to zero. Accordingly in Fig. 5 we have shown the results up to  $N=56$  to emphasize this point. Also, for our purpose we shall neglect this small difference in the drip line mentioned above.

Fig. 5 also shows the results of RCHB calculations of Ref. 26 carried out with the NL-SH force parameterization. A comparison with these results shows that the RMF+BCS description is almost similar to that of the RCHB results. From fig. 5 it is evident that our RMF+BCS results obtained with the NL-SH force, in contrast to those for the TMA force, are closer to the RCHB results which are also obtained using the NL-SH force. The upper panel of the figure explicitly shows the difference in the separation energy obtained in the RCHB and the RMF+BCS calculations for the NL-SH force. Indeed the difference is quite small. This figure also depicts the difference of calculated values with respect to the available experimental data for the separation energy. The maximum difference is of the order of less than 2 MeV. However, it should be emphasized that the difference with respect to the experimental data for both the RMF+BCS and the RCHB calculations are of similar nature as is easily seen in the figure.

The rms radii for the proton and neutron,  $r_{p,n} = (\langle r_{p(n)}^2 \rangle)^{1/2}$  calculated from the respective density distributions are obtained from

$$\langle r_{p(n)}^2 \rangle = \frac{\int \rho_{p(n)} r^2 d\tau}{\int \rho_{p(n)} d\tau} \quad (7)$$

The experimental data for the rms charge radii are used to deduce the nuclear rms proton radii using the relation  $r_c^2 = r_p^2 + 0.64 fm^2$  for the purpose of comparison. In the lower panel of fig. 6a we have shown the results for the neutron and proton rms radii of the Ca isotopes obtained with the NL-SH force. For the purpose of comparison the figure also depicts the results of RCHB calculations<sup>26</sup> carried out with the same NL-SH force. A comparison of the RMF+BCS results with that for the RCHB shows that the two approaches yield almost similar values for the neutron and proton rms radii  $r_n$  and  $r_p$ .



**Fig. 6a.** The present RMF results for the rms radii of neutron  $r_n$  and proton  $r_p$  (lower panel) for the Ca isotopes obtained with the NL-SH (open squares) force parameters are compared with the continuum relativistic Hartree-Bogoliubov (RCHB) calculations of Ref. 26 carried out with the NL-SH force (open triangles). The upper panel depicts the difference between the results obtained from RMF+BCS and the RCHB approaches for the proton, and the neutron rms radii using the NL-SH force.

We have not plotted in fig. 6a the results obtained with the TMA force as it is found that the calculated values for these radii using two different forces, TMA and the NL-SH, are almost similar to each other. Instead the TMA results are shown separately in fig. 6b along with the available experimental data to keep the figure uncluttered. In fact experimental data for the proton and neutron rms radii are available only for a few stable Ca isotopes as is seen from fig. 6b. It is evident that the measured proton radii  $r_p$  for the isotopes  $^{40-48}\text{Ca}$  are in excellent agreement with our RMF+BCS results. Similarly the neutron radii  $r_n$  for the  $^{40,42,44,48}\text{Ca}$  isotopes are found to compare reasonably well, though for the  $^{40,42}\text{Ca}$  isotopes the calculated values are slightly lower than the measured ones as is seen in the figure.

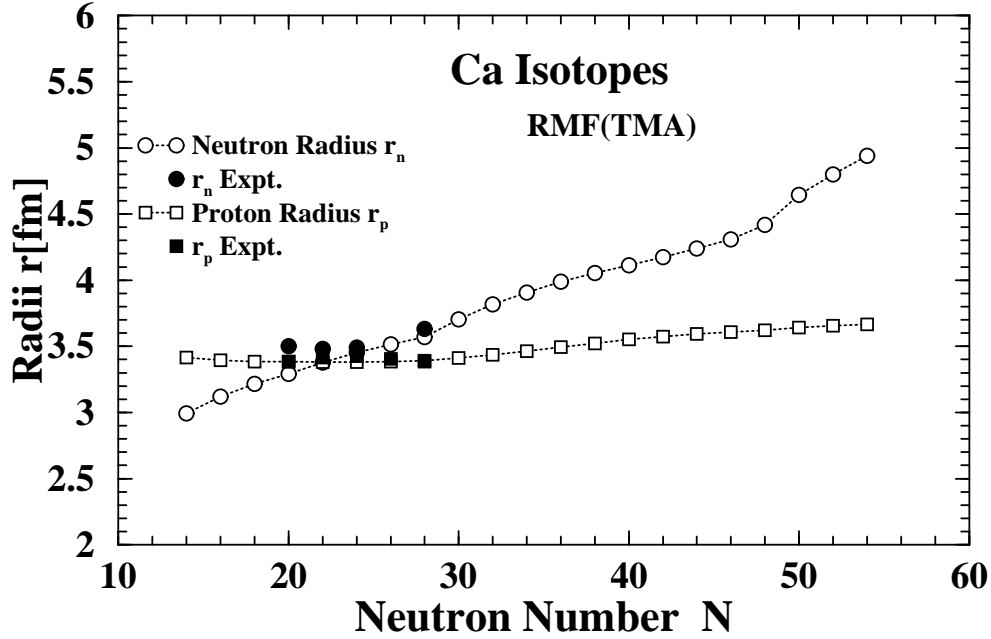


**Fig. 6b.** The present RMF results for the rms radii of neutron distribution  $r_n$  (open circles), and that of proton distribution  $r_p$  (open squares) for the Ca isotopes obtained with the TMA force parameters are compared with the available experimental data <sup>34</sup>, shown by solid circles and solid squares, respectively.

In order to provide a more quantitative comparison of RMF+BCS and the RCHB calculations, we have plotted in the upper panel of fig. 6a the differences  $\Delta r_p$  and  $\Delta r_n$  for the proton and neutron rms radii obtained using the RMF+BCS and RCHB approaches with NL-SH force. These results have been, respectively, shown by opened circles and diamonds for the neutron and by opened squares and triangles for the proton. It is seen from the figure that the difference between the results of RMF+BCS and RCHB calculations for the proton and neutron radii are rather quite small. Indeed, the maximum difference of about 0.15 Fermi is found for the extremely neutron rich isotopes ( $A \geq 70$ ) at the top of the drip-line wherein already the halo like formation has taken place and radii are rather quite large. Indeed it is clearly seen that the value of  $\Delta r_p$  and  $\Delta r_n$  for the RMF+BCS and RCHB approaches are of the order of 1 – 2% and 2 – 5%, respectively. Similarly it is found that this difference for the RMF+BCS using two different forces (not shown in the figure) is of the order of about 3 – 5% for the proton and 3 – 6% for the neutron rms radii, respectively.

As described earlier, in the case of neutron rich Ca isotopes the neutron  $1g_{9/2}$  state happens to be one of the main resonant states having good overlap with the bound states near the Fermi level. This causes the pairing interaction to scatter particles from the neighboring bound states to the resonant state and vice versa. Thus, it is found that the resonant  $1g_{9/2}$  state starts being partially occupied even

before the lower bound single particle states are fully filled in. This property of the resonant states is observed throughout for all the nuclei considered in the present investigation. However, in the case of neutron rich Ca isotopes it is found that the neutron  $3s_{1/2}$  state which lies close to the  $1g_{9/2}$  state also starts getting partially occupied before the  $1g_{9/2}$  state is completely filled. The neutron  $3s_{1/2}$  state due to lack of centrifugal barrier contributes more to the neutron rms radius as compared to the  $1g_{9/2}$  state, and thus one observes a rapid increase in the neutron rms radius shown in fig. 6a beyond the neutron number  $N = 42$  indicating the halos like formation. A comparison of the rms neutron radii with the  $r_n = r_0 N^{1/3}$  line shown in the figure suggests that these radii for the drip-line isotopes do not follow the simple  $r_0 N^{1/3}$  systematics.

An important aspect of the heavy neutron rich nuclei is the formation of the neutron skin.<sup>1</sup> For the nucleus  $^{66}\text{Ca}$  this characteristic feature is seen in Fig. 7, where we plot the radial density distribution for protons by hatched lines and that for the neutrons by solid line. The figure also shows the neutron density distributions for the other two isotopes  $^{56,64}\text{Ca}$ . The neutron density distributions in the neutron rich  $^{62-72}\text{Ca}$  nuclei are found to be widely spread out in the space and give rise to the formation of neutron halos as will be discussed later.

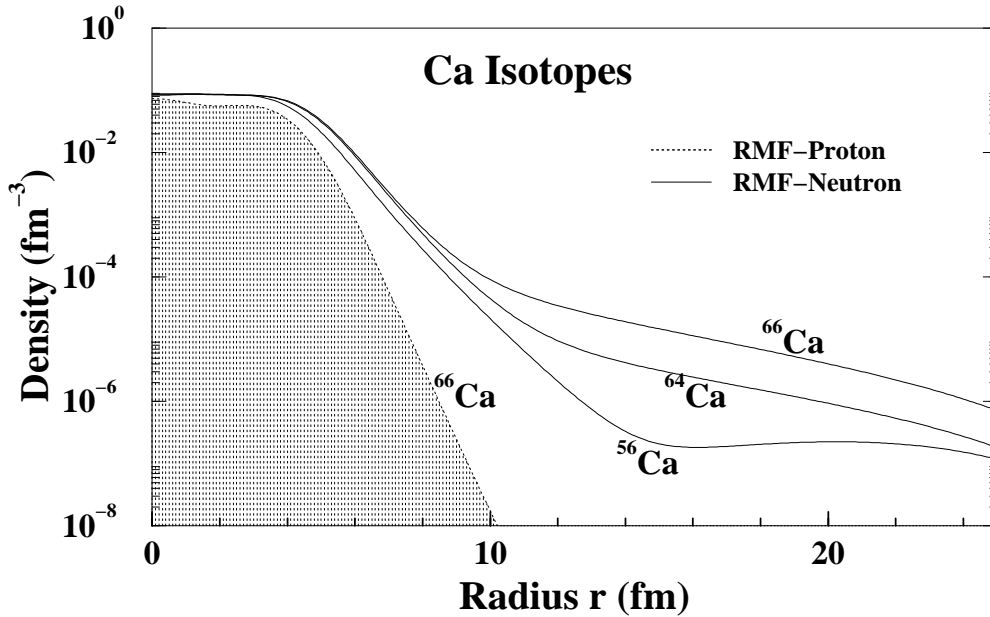


**Fig. 7.** Results for the proton and neutron density distributions obtained in the RMF+BCS calculations employing the TMA force. The radial proton density distribution for the isotope  $^{66}\text{Ca}$  has been shown by the hatched area. The neutron radial density distribution for the  $^{56,64,66}\text{Ca}$  isotopes have been shown by solid lines.

A typical example of variation in the proton radial density distributions with

increasing neutron number has been shown in fig. 8 for the NL-SH force calculations. As is seen in the figure the proton distributions are observed to be confined to smaller distances. Moreover, these start to fall off rapidly already at smaller distances (beyond  $r > 3$  fm.) as compared to those for the neutron density distributions. In the interior as well as at outer distances the proton density values are larger for the proton rich Ca isotopes and decrease with increasing neutron number  $N$ . However, in the surface region, ( $r \approx 4$  fm), the proton density values reverse their trend and increase with increasing neutron number. Due to this feature of the proton density distributions the proton radii are found to increase, albeit in a very small measure, with increasing neutron number though the proton number is fixed at  $Z = 20$  for the Ca isotopes. Similar features of the proton density distributions are also exhibited by the results obtained with the TMA force parametrization. From fig. 7 it is observed that the neutron density distributions have wide spatial extension, and with increasing neutron number the density values are appreciably increased. The asymptotic behavior of the densities are influenced by the positive energy quasi bound states via the pairing correlations. For the closed shell Ca isotopes ( $N = 14, 20, 28$  and  $40$ ), due to absence of this correlation, the calculations yield sharply falling asymptotic density distribution as is discussed below.

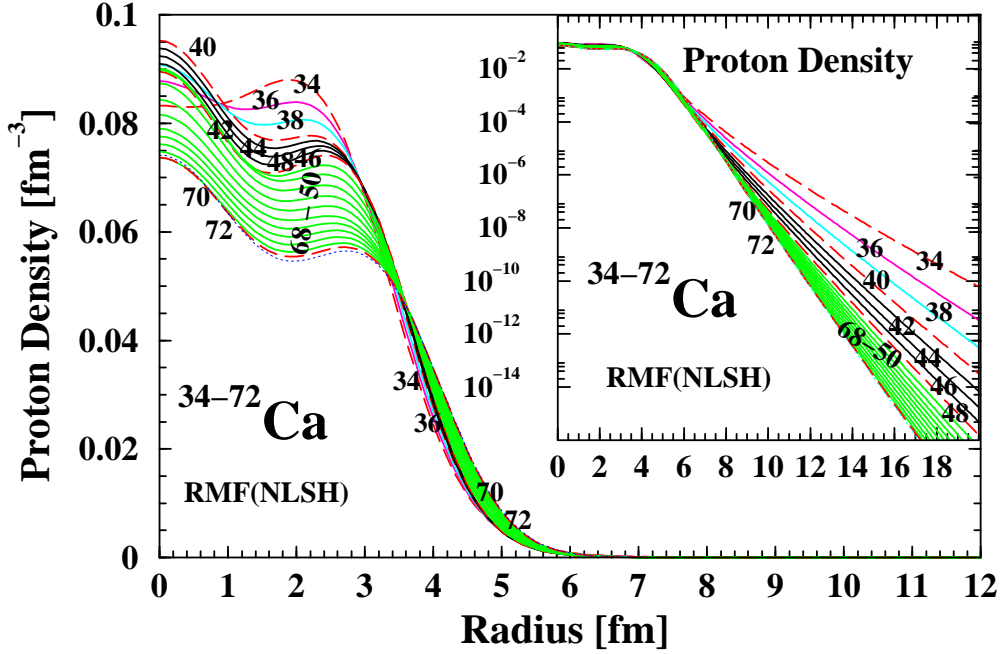


**Fig. 8.** Results for the proton density distributions for the Ca isotopes obtained in the RMF+BCS calculations employing the NL-SH force. The numbers on the density distribution lines indicate the mass number of the Ca isotope.



## 3.1.1. Halo Formation in Ca Isotopes

For the purpose of illustration, we have displayed in Fig. 9 the detailed neutron density profile obtained with the TMA force for the Ca isotopes. In our earlier discussions for the Ca isotopes, it has been observed from the neutron dependence properties that the neutron numbers  $N = 14, 20, 28$  and  $40$  correspond to closed shells, and thus, represent the magic numbers for these isotopes. This conclusion is found to be consistent with the calculated densities shown in fig. 9 for the isotopes corresponding to these neutron numbers. Evidently for  $N = 14, 20, 28$  and  $40$  the neutron densities fall off rapidly and have smaller tails as compared to the isotopes with other neutron numbers. As remarked earlier this sharp fall in asymptotic density values is due to the fact that for the closed shell isotopes there are no contribution to the density from the quasi bound states having positive energy albeit close to zero energy near the continuum threshold.

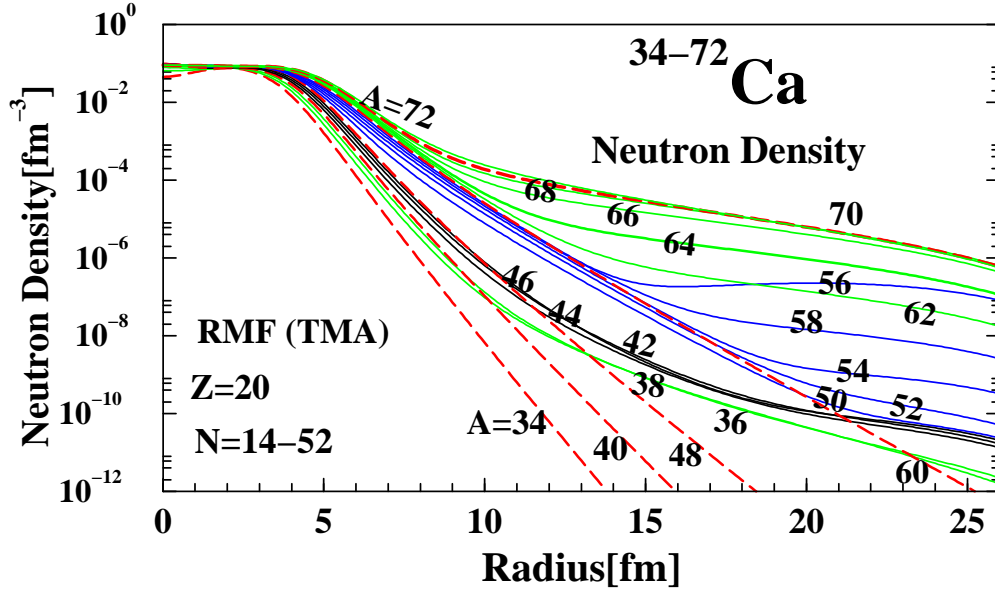


**Fig. 9.** The neutron radial density distribution for the  $^{34-72}\text{Ca}$  isotopes obtained in the RMF+BCS calculations using the TMA force. The rapidly falling density distributions correspond to isotopes with neutron magic numbers at  $N = 14, 20, 28$  and  $40$ , and have been shown by the dashed lines whereas for the other isotopes these are plotted as solid lines.

The density distribution for the  $N = 50$  case (corresponding to  $^{70}\text{Ca}$ ) is seen to be very different from those of the isotopes with  $N = 14, 20, 28$  and  $40$  indicating thereby that for the neutron rich Ca isotopes the neutron number  $N = 50$  does not correspond to a magic number. The neutron single particle spectrum for the  $^{70}\text{Ca}$  isotope shows that apart from the bound states and high lying resonant states

(the lower  $1g_{9/2}$  resonant state has already become bound for this isotope), the positive energy neutron states  $2d_{5/2}$ ,  $2d_{3/2}$ ,  $4s_{1/2}$ ,  $3p_{3/2}$ ,  $3p_{1/2}$ ,  $3d_{5/2}$ ,  $3d_{3/2}$ , all lying very close to the neutron Fermi level ( $\epsilon_f = 0.08$  MeV), are also being occupied. The occupation probabilities for these positive energy states are indeed very small. However, a sum of all these accounts for about 0.6 nucleon occupying the positive energy states. Out of this, the  $2d_{5/2}$  state lying closest to the Fermi level at  $\epsilon = 0.47$  MeV has the maximum occupancy weight which amounts to about 0.55 nucleon being in this energy state. The contribution to the total density distribution for the  $^{70}\text{Ca}$  isotope ( $N = 50$ ) from these positive energy states consequently modifies the asymptotic density distribution. Thus in contrast to the closed shell isotopes, here the density does not fall off rapidly with increasing radial distances. This feature of the density profile can be essentially attributed to loosely bound states like the  $2d_{5/2}$  in the  $^{70}\text{Ca}$  isotope. This effect is seen to persist in all the isotopes irrespective of being neutron rich or poor, exceptions being those with closed shells wherein the pairing correlations are not able to populate the positive energy states.

Next we consider a comparison of results obtained with the TMA and NL-SH forces, and also of those obtained using the RCHB approach. Results of calculations using the NL-SH force are found to be almost similar to those obtained with the TMA Lagrangian already shown in fig. 9. Also it is found that the RMF+BCS results for the proton and neutron densities are almost similar to those obtained in the RCHB approach. For the purpose of illustration we have plotted in fig. 10 the results for the neutron densities obtained in the RMF+BCS calculations (solid lines), and those obtained in the RCHB calculations (dashed lines) again using the NL-SH force for the purpose of comparison. It is seen from the figure that the results from both, the RMF+BCS and the RCHB, approaches for the neutron density distributions are almost similar. In particular, for the isotopes with neutron shell closure corresponding to  $N = 14, 20, 28$  and  $40$  this similarity extends up to large radial distances whereby the densities are already diminished to very small values, rather less than  $10^{-10} \text{ fm}^{-3}$ . This has been explicitly demonstrated in the inset of fig. 10 which shows the results on a logarithmic scale for radial distances up to  $r = 16$  fm. For the other isotopes, there are small deviations between the RMF+BCS and the RCHB approaches beyond the radial distance  $r = 8$  fm. However, beyond this distance the densities are already quite reduced ranging between  $10^{-4} \text{ fm}^{-3}$  to  $10^{-8} \text{ fm}^{-3}$ . These small deviations between the RMF+BCS and RCHB results beyond  $r = 8$  fm is caused due to small differences in the single particle energies and wave functions, especially near the Fermi surface, and also on the energy cut off being used in the RCHB calculations. Nevertheless, similarities between the RMF+BCS and the RCHB results are exceedingly encouraging.

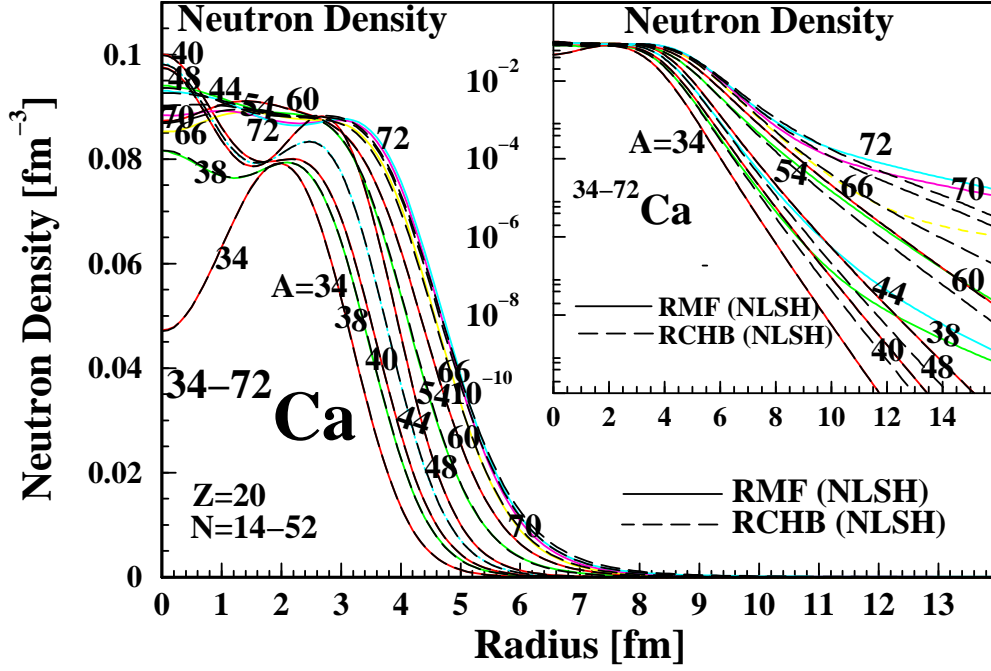


**Fig. 10.** The solid line show the neutron radial density distribution for the  $^{34-72}\text{Ca}$  isotopes obtained in the RMF+BCS calculations using the NL-SH force. Corresponding results of the RCHB calculations with the NL-SH force are shown by the dashed lines for the purpose of comparison. The inset shows the results on a logarithmic scale up to rather large radial distances.

In fig. 10, it is interesting to note that the neutron density distributions, outside the nuclear surface and at large distances, for the neutron rich Ca isotopes with neutron number  $N \geq 42$  are larger by several orders of magnitude as compared to the lighter isotopes. This behavior of the density distribution for the neutron rich Ca isotopes is quite different from the corresponding results, especially for the neutron rich isotopes of Ni, Sn and Pb nuclei. In the latter cases, as more neutrons are added the tail of the neutron density distributions for the neutron rich isotopes tends to saturate. The results described above can be easily understood by inspecting the variation in the position of the single particle states and that of the Fermi energy with increasing neutron number depicted in fig. 11.

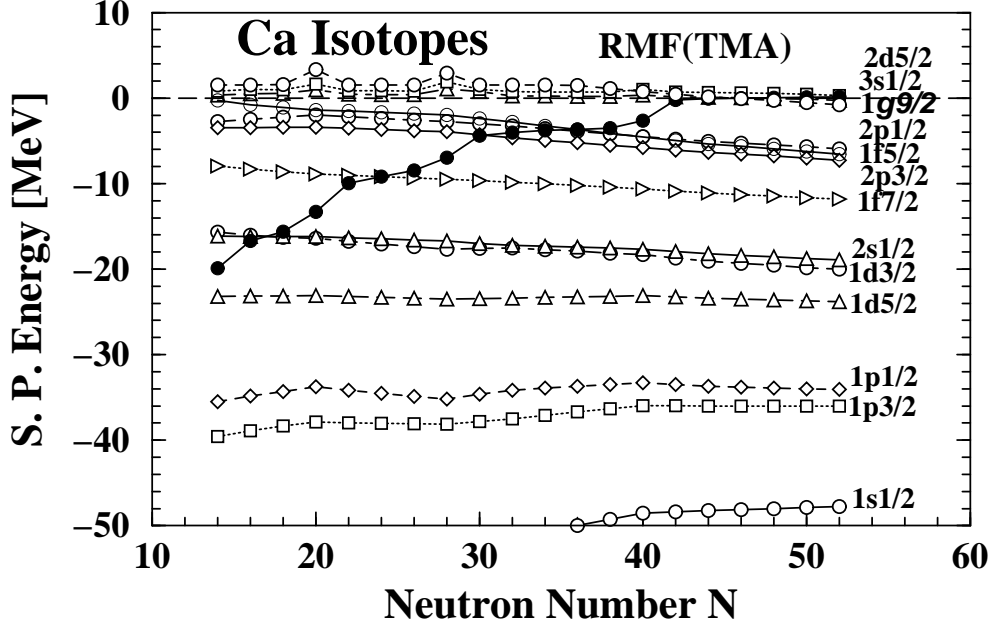


**Fig. 11.** Variation of the neutron single particle energies obtained with the TMA force for the Ca isotopes with increasing Neutron number. The Fermi level has been shown by filled circles connected by solid line to guide the eyes.

First of all, it is readily seen in fig.11 that the large energy gaps between single particle levels  $1d_{5/2}$  and  $1d_{3/2}$ , and the levels  $2p_{1/2}$  and  $3s_{1/2}$  etc. are responsible for the properties akin to shell or sub-shell closures in the  $^{34-72}\text{Ca}$  isotopes for the neutron number  $N = 14$  and  $40$  apart from the traditional magic nos.  $N = 20$  and  $28$ . However the  $N = 50$  shell closure is seen to disappear due to absence of gaps between the  $1g_{9/2}$  state and the states in the s-d shell.

For an understanding of the halo formation in the neutron rich ( $N \geq 42$ ) Ca isotopes we next look into the detailed features of single particle spectrum and its variation as one moves from the lighter isotope to heavier one in fig. 11. The neutron Fermi energy which lies at  $\epsilon_f = -19.90$  MeV in the neutron deficient  $^{34}\text{Ca}$  nucleus moves to  $\epsilon_f = -0.21$  MeV in the neutron rich  $^{62}\text{Ca}$ , and to  $\epsilon_f = 0.08$  MeV (almost at the beginning of the single particle continuum) in  $^{70}\text{Ca}$ . The  $1g_{9/2}$  state which lies at higher energy in continuum for the lighter isotopes, (for example at  $\epsilon = 1.68$  MeV in  $^{34}\text{Ca}$ ) comes down gradually to become slightly bound, ( $\epsilon = -0.07$  MeV in  $^{66}\text{Ca}$ ) for the neutron rich isotopes. Similarly, the  $3s_{1/2}$  state which lies in continuum for the lighter isotopes (for example at  $\epsilon = 0.70$  MeV in  $^{34}\text{Ca}$ ) also comes down, though not so drastically, to become slightly bound ( $\epsilon = -0.05$  MeV in  $^{68}\text{Ca}$ ) for the neutron rich isotopes. In the case of  $^{60}\text{Ca}$  with shell closure for both protons and neutrons, the neutron single particle states are filled in up to the  $2p_{1/2}$  state, while the next high lying states  $3s_{1/2}$  and  $1g_{9/2}$ , separated by about 5 MeV from the  $2p_{1/2}$  level are completely empty. Now on further addition of 2

neutrons, it is observed that the  $1g_{9/2}$  is filled in first even though  $3s_{1/2}$  state is slightly lower (by about 0.31 MeV) than the  $1g_{9/2}$  state as has been shown in fig. 12. Still another addition of 2 neutrons are found to fill in the  $1g_{9/2}$  state once again, though now the  $1g_{9/2}$  state is higher to the  $3s_{1/2}$  state merely by 0.08 MeV. This preference for the  $1g_{9/2}$  state results in the existence of loosely bound highly neutron rich Ca isotopes. Indeed this preference stems from the fact that in contrast to the  $3s_{1/2}$  state, the positive energy  $1g_{9/2}$  state being a resonant state has its wave function entirely confined inside the potential well akin to a bound state. This has been shown earlier in fig. 2 for the nucleus  $^{62}\text{Ca}$ . As is evident from fig. 2, the  $3s_{1/2}$  state in the continuum has its wave function spread over mostly outside the potential well and thus the additional neutrons do not occupy this state until it becomes a bound state.

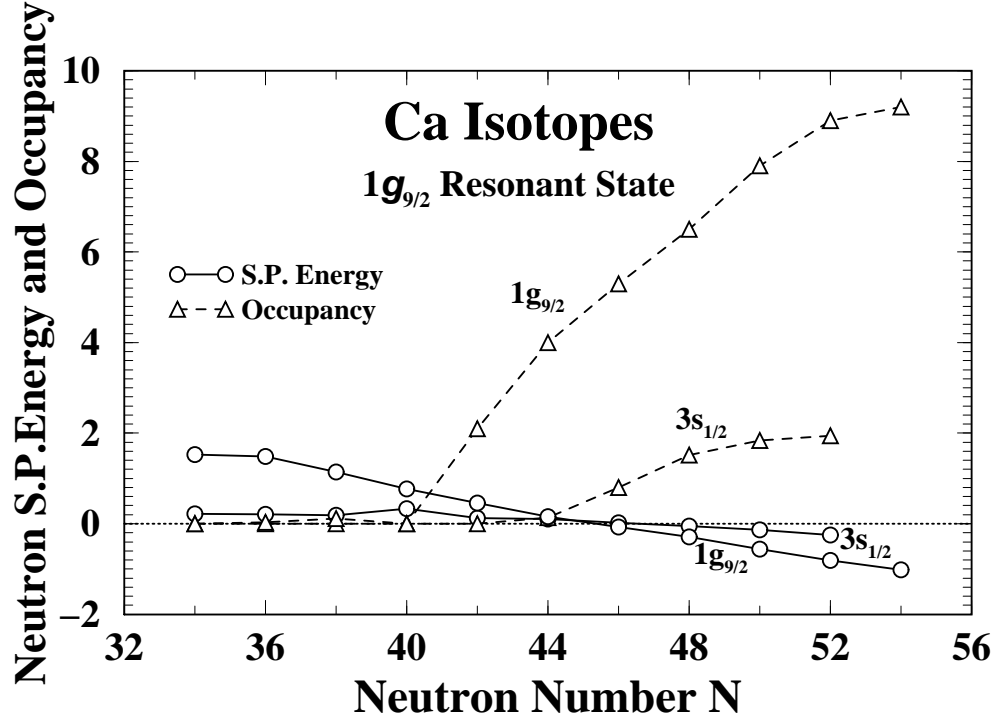


**Fig. 12.** Variation in energy shown by open circles, and occupancy (no. of neutrons occupying the levels) depicted by open triangles for the neutron  $1g_{9/2}$  and  $3s_{1/2}$  single particle states in the Ca isotopes.

For the neutron number  $N = 48$ , it is found that both the  $1g_{9/2}$  and  $3s_{1/2}$  states become bound and start to compete together to get occupied on further addition of neutrons as can be seen in fig. 12. On the other hand, the positive energy states like  $2d_{5/2}$ ,  $2d_{3/2}$ ,  $3p_{3/2}$  and  $3p_{1/2}$  lying near the Fermi level at the continuum threshold are also being occupied though with very small probability. Further it is observed

from the figure that both of these states are completely filled in for the neutron number  $N = 52$ , and thus, the neutron drip line is reached with a loosely bound  $^{72}\text{Ca}$  nucleus. The next single particle state,  $2d_{5/2}$ , is higher in energy by about 0.5 MeV in the continuum and further addition of neutrons does not produce a bound system.

As mentioned above, the  $1g_{9/2}$  state is mainly confined to the potential region, and hence its contribution to the neutron radii is similar to a bound state. In contrast, the  $3s_{1/2}$  state which has no centrifugal barrier, and thus, is spread over large spatial extension contributes substantially to the neutron density distribution at large distances. Similarly it turns out that the  $3p_{1/2}$  state though to a lower extent contributes to the extended density distribution. Due to this reason, for  $N > 42$  as the  $3s_{1/2}$  state starts being occupied the neutron density distribution has large tails, and the neutron radii for the neutron rich isotopes ( $N > 42$ ) grow abruptly as has been shown in fig. 6. Thus the filling of the  $3s_{1/2}$  single particle state and to a lesser extent that of  $2d_{5/2}$ ,  $3p_{3/2}$  and  $3p_{1/2}$  etc. with increasing neutron number in the  $^{64-72}\text{Ca}$  isotopes causes the neutron halos like formation in these nuclei.

### 3.2. Ni *Isotopes*

Results for the Ni isotopes exhibit similar characteristics for the pairing gap contribution due to the resonant states, and those from other single particle states near the Fermi level. However, the neutron rich Ni isotopes do not exhibit a situation like the neutron rich Ca isotopes favoring for halo formation. This is due to difference in the single particle structure near the Fermi surface as will be discussed later. In order to illustrate the physical situation of neutron rich Ni isotopes, we have plotted in fig. 13 the RMF potential (upper panel), and some of the single particle wave functions (lower panel) for the nucleus  $^{84}\text{Ni}$ . The upper panel also shows the spectrum for the neutron bound single particle states, and a few of the positive energy states in the continuum. Some of the most relevant neutron single particle states close to the neutron Fermi level, which are found to be important for the description of neutron rich Ni isotopes near the drip line are:  $4s_{1/2}$ ,  $3p_{3/2}$ ,  $3p_{1/2}$ ,  $1g_{7/2}$ ,  $2d_{5/2}$  and  $2d_{3/2}$ . Analogous to the  $1g_{9/2}$  state for the case of neutron rich Ca isotopes, the neutron  $1g_{7/2}$  state is found to be the most important resonant state for the Ni isotopes. It has been shown in the figure along with the positive energy  $4s_{1/2}$ ,  $3p_{3/2}$ ,  $3p_{1/2}$  states mentioned above. In addition, we have also depicted in fig. 13 the total mean field potential for the resonant  $1g_{7/2}$  state, obtained by adding the centrifugal potential energy. Once again, many states high lying in the continuum have not been shown in the figure. Also in fig. 13 (lower panel), we have displayed the radial wave functions of some of the neutron single particle states close to the Fermi surface, the neutron Fermi energy being  $\lambda_n = -1.21$  MeV. These include the bound  $2d_{3/2}$  and the continuum  $3p_{3/2}$ ,  $4s_{1/2}$  and  $1g_{7/2}$  single particle states.

It is seen from fig. 13 that the resonant neutron  $1g_{7/2}$  state in the neutron rich Ni isotopes, similar to the resonant state in the Ca isotopes, remains mainly confined to the region of the potential well and the wave function exhibits characteristics similar to that of a bound state. Also, it is evident from the figure that, in contrast to the resonant state  $1g_{7/2}$ , the wave function for a typical non-resonant state, for

example  $3p_{3/2}$ , is well spread over to large distances outside of the potential region. Such states thus have a small overlap with the bound states near the Fermi surface leading to diminished value for the pairing gaps for these states. The next important states are the loosely bound states. A representative example of such a state is the  $2d_{3/2}$  state at  $-0.55$  MeV. From fig. 13 it is seen that this state has a sizable part of the wave function within the region of the potential well, and for such states the pairing gap values, as has been shown in fig. 14, are found to be comparable to the bound states making significant contributions to the pairing energy.

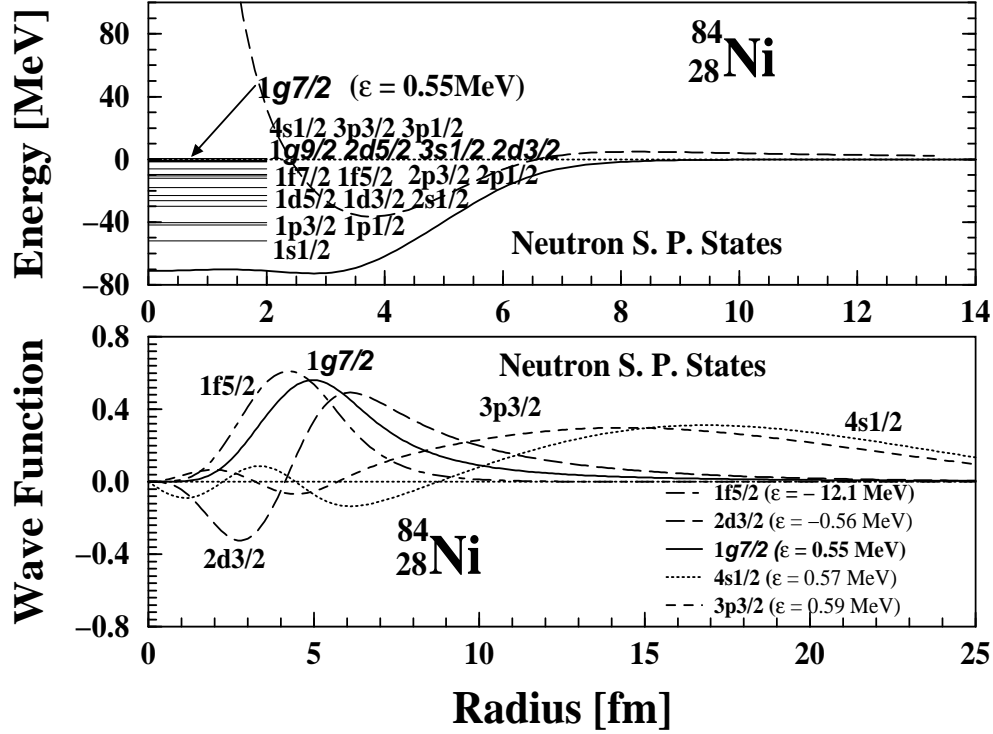


**Fig.13.** Upper panel: The RMF potential energy (sum of the scalar and vector), for the nucleus  $^{84}\text{Ni}$  as a function of radius is shown by the solid line. The long dashed line represents the sum of RMF potential energy and the centrifugal barrier energy for the neutron resonant state  $1g_{7/2}$ . The figure also shows the energy spectrum of the bound neutron single particle states along with the resonant  $1g_{7/2}$  state at  $0.55$  MeV.

Lower panel: Radial wave functions of a few representative neutron single particle states with energy close to the Fermi surface for the nucleus  $^{84}\text{Ni}$ . The solid line shows the resonant  $1g_{7/2}$  state at energy  $0.55$  MeV, while the bound  $2d_{3/2}$  state at  $-0.56$  MeV is shown by long dashed line. The  $4s_{1/2}$  and  $3p_{3/2}$  states with positive energies  $0.57$  MeV and  $0.59$  MeV have been depicted by dotted and small dashed lines, respectively

The next resonance above  $1g_{7/2}$  is a  $1h_{11/2}$  state. This resonance appears quite high in energy, at  $E = 4.6$  MeV, and has a width of about  $0.13$  MeV. We estimated the position and the width of this resonance by calculating the phase shift corre-

sponding to the RMF single particle potential. It is worth mentioning that in a box calculation one could find always a  $1h_{11/2}$  state at approximately 4.5 MeV, but the order of its appearance depends on the box radius. However, after inclusion of the  $1h_{11/2}$  state, it is found the results remain essentially unchanged. Indeed, its contribution is much smaller than that of the  $1g_{7/2}$  state due to the large energy difference of the  $1h_{11/2}$  state with respect to the Fermi level.

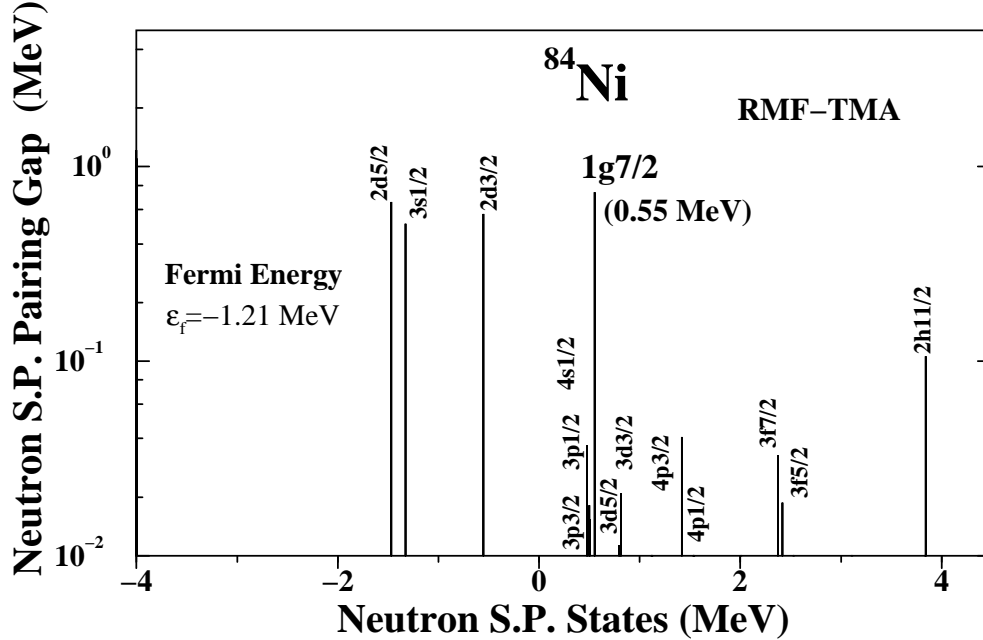


**Fig. 14.** Pairing gap energy  $\Delta_j$  of neutron single particle states with energy close to the Fermi surface for the nucleus  $^{84}\text{Ni}$ . The resonant  $1g_{7/2}$  state at energy 0.55 MeV has the gap energy of about 1 MeV which is close to that of bound states like  $2d_{5/2}$  etc.

The pairing gap values obtained in our RMF+BCS calculations as shown in fig 14 turn out to be of the order of 1 MeV and are consistent with the results of other mean field calculations and those deduced from experimental data on the binding energies.<sup>4,20,30,32</sup> The RHB calculations of Lalazissis et al.<sup>20</sup> have been carried out using the finite range Gogny interaction D1S<sup>31</sup> for the treatment of pairing correlations. These calculations provide the average values of canonical pairing gaps as function of canonical single particle energies. These RHB averaged canonical gaps correspond to the pairing gaps in BCS theory, although the two are not completely equivalent. In the publication of Lalazissis et al.<sup>20</sup> detailed results for the gaps are available only for the  $^{70}\text{Ni}$  isotope. The averaged gaps decrease approximately monotonically with increasing single particle energies and have values ranging from about 2.2 MeV for the deep hole states, to about 0.5 MeV for the high lying states in the continuum. In comparison to these values our RMF+BCS calculations yield a little smaller gaps ranging from about 1.2 MeV



for the well bound states, to about 0.8 MeV for the continuum states near the Fermi surface. Similarly, the HFB calculations of Dobaczewski et al.<sup>4</sup> have been carried out using three different interactions for the pairing correlations. These are the finite range density dependent Gogny interaction D1S<sup>31</sup>, the effective Skyrm interaction<sup>2,32</sup> SKP, and the interaction SKP <sup>$\delta$</sup>  which uses SKP parametrization in the p-h channel and a  $\delta$ -interaction for the pairing component. These extensive calculations carried out for the Sn isotopes show that the results for the HFB with D1S interaction overestimate the gap values as compared to those obtained with either the SKP or the SKP <sup>$\delta$</sup>  interaction. Indeed our calculated gaps for the Sn isotopes are found to be very close to those of HFB using the SKP <sup>$\delta$</sup>  interaction as will be elaborated later while discussing the results of Sn isotopes. With this in view, our RMF+BCS results seem quite consistent with RHB and HFB calculations using similar pairing interaction.

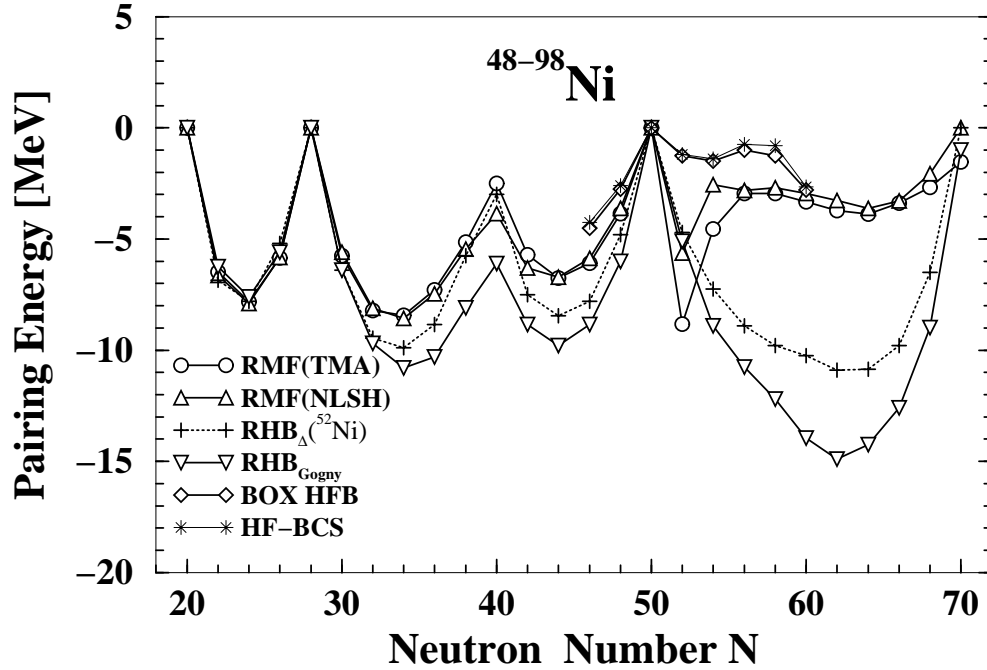


**Fig. 15.** Present RMF results for the pairing energy for the  $^{48-98}\text{Ni}$  isotopes obtained with the TMA (open squares) are compared with those obtained using the NL-SH (open triangles) force parameters. The results of different RHB calculations (see text for details) are also shown for the purpose of comparison.

In fig. 15 we compare our results for the contribution to the pairing energy with those obtained using other mean-field approaches for the  $^{48-98}\text{Ni}$ . The choice of comparison with the  $^{48-98}\text{Ni}$  isotopes is guided by the fact that for these nuclei several theoretical results are available. As before, our RMF+BCS calculations using the TMA and NL-SH forces yield similar values for the pairing energy. These

two results have been shown in fig. 15 by open circles and triangles, respectively. Further, we note that the pairing energy vanishes for the nuclei with neutron numbers  $N = 20, 28, 50$  and  $70$  indicating shell closure for these neutron numbers. This indicates the appearance of new shell corresponding to neutron number  $N = 70$ . The variation of the neutron pairing energy with the neutron number  $N$  exhibits features well known from the case of stable nuclei. Thus, as expected, between the two neutron magic numbers the pairing energy increases in magnitude from zero to reach a maximum for the half filled shell nuclei. In the present case, the pairing energy for the neutron half filled shell nuclei is found to vary between  $-10$  MeV for  $N = 24$  and  $-15$  MeV for the neutron rich case with  $N = 62$  as seen in fig. 15. Also, it is observed from this figure that  $N=40$  represents a sub-shell with a small value of total pairing energy which is approximately  $3$  MeV.

We have also plotted in fig. 15, for the purpose of comparison, the results of RHB calculations carried out with a zero range delta force, shown by plus symbols, and that with the finite range Gogny interaction<sup>30</sup> depicted by inverted triangles. Also, are shown the results obtained in the continuum HF-BCS, depicted by stars, and the Box HFB calculations, depicted by diamonds, of Grasso et al.<sup>7</sup>. The RMF+BCS results for the  $N$  dependence of the pairing energy exhibit similar trend as those obtained from the RHB calculations, However, the values of the pairing energy for the neutron rich nuclei are rather large in the case of RHB calculations as is seen in fig. 15. The results for the continuum HF-BCS and HFB calculations, though available only for limited isotopes<sup>7</sup>, are closer to our calculations.

In fig. 16 we plot the results of two neutron separation energy for the entire chain of Ni isotopes up to the neutron drip-line. The figure also shows the HFB results of Terasaki *et al.*<sup>3</sup> and that of the RHB calculations of Ref. 19, along with the experimental data available<sup>25</sup> for the <sup>50-78</sup>Ni isotopes. Since the RHB calculations of Ref. 20 are performed only for  $24 \leq N \leq 50$  and because these results are similar to that of the RHB calculations of Ref. 19, we have shown in Fig. 16 only the results of Ref. 19. Further, we have chosen the calculations in Ref. 3 using the HFB theory to be a representative one, therefore the results of other HFB calculations<sup>4,21</sup> are not depicted in the figure. It is gratifying to note that our RMF results are in excellent agreement with the data. The strong variations in the experimental separation energy near the neutron magic numbers  $N = 28, 50$  are well accounted for by our calculations. The figure shows that the overall trends of results obtained using different theories are similar, though there are minor differences in details. However, it is clearly seen that the RHB calculations compare very well with our results for the two neutron separation energy and the slope of the curve all the way up to  $A=100$  in the two cases are very similar. This good agreement with the RHB results<sup>19,20</sup> provides another strong support, in addition to that of the HF+BCS calculations with continuum of Ref. 6, to the validity of a RMF+BCS approach for the investigation of the drip-line nuclei.

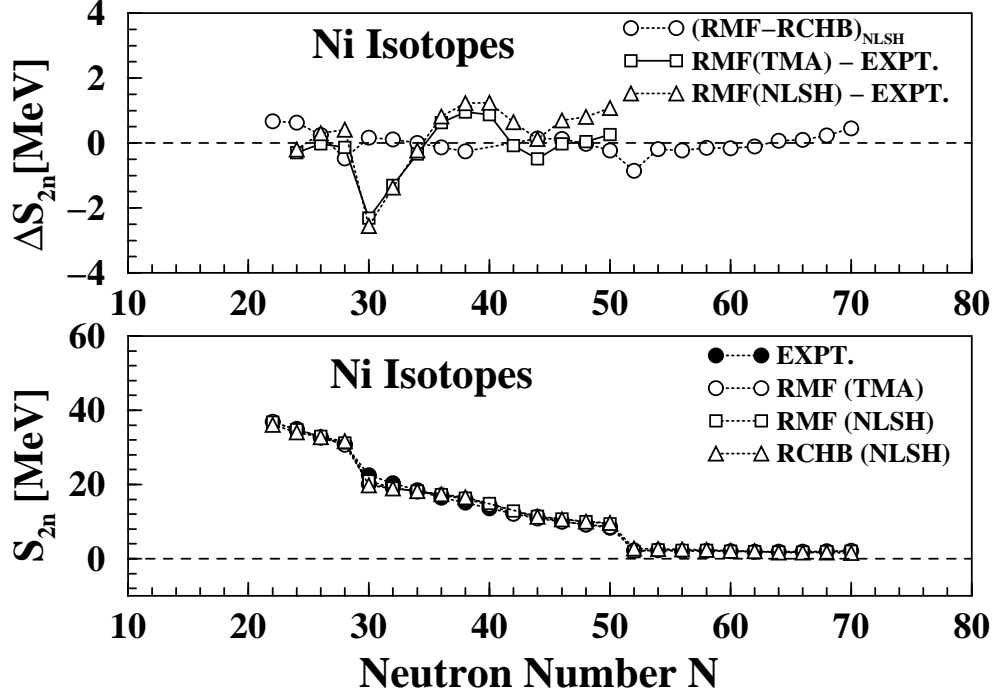


**Fig. 16.** In the lower panel the present RMF results for the two neutron separation energy for the  $^{50-98}\text{Ni}$  isotopes obtained with the TMA (open circles) and the NL-SH (open squares) force parameters are compared with the continuum relativistic Hartree-Bogoliubov (RCHB) calculations of Ref. 26 carried out with the NL-SH force (open triangles). The lower panel also depicts the available experimental data<sup>25</sup> ( $^{50-78}\text{Ni}$ ) for the two neutron separation energy (solid circles) for the purpose of comparison. The upper panel depicts the difference in the RMF+BCS results and the RCHB results of Ref. 26 obtained for the NL-SH force. This part of the figure also shows the difference of the calculated results with respect to the available experimental data<sup>25</sup>.

In both relativistic calculations, i.e. RMF+BCS and RCHB, the two-neutron drip line is predicted at  $A=98$  ( $N=70$ ). This is quite different from the result of non-relativistic HFB calculations of Ref.<sup>3</sup>, which predicts the two-neutron drip line around  $A=90$  ( $N=62$ ). This difference between the two predictions can be traced back to the spin orbit splitting of the neutron  $1g_{9/2}$  and  $1g_{7/2}$  states, which is smaller in the relativistic calculations. Thus in RMF+BCS the positive energy state corresponding to the  $1g_{7/2}$  resonance is much closer to the continuum threshold than in the HFB calculations and is becoming a bound states beyond  $N=58$  as has been shown in fig. 17. Consequently, in variance with HFB, in RMF+BCS calculations one can put 8 neutrons more on the bound state  $1g_{7/2}$  before we reach the two neutron drip line.

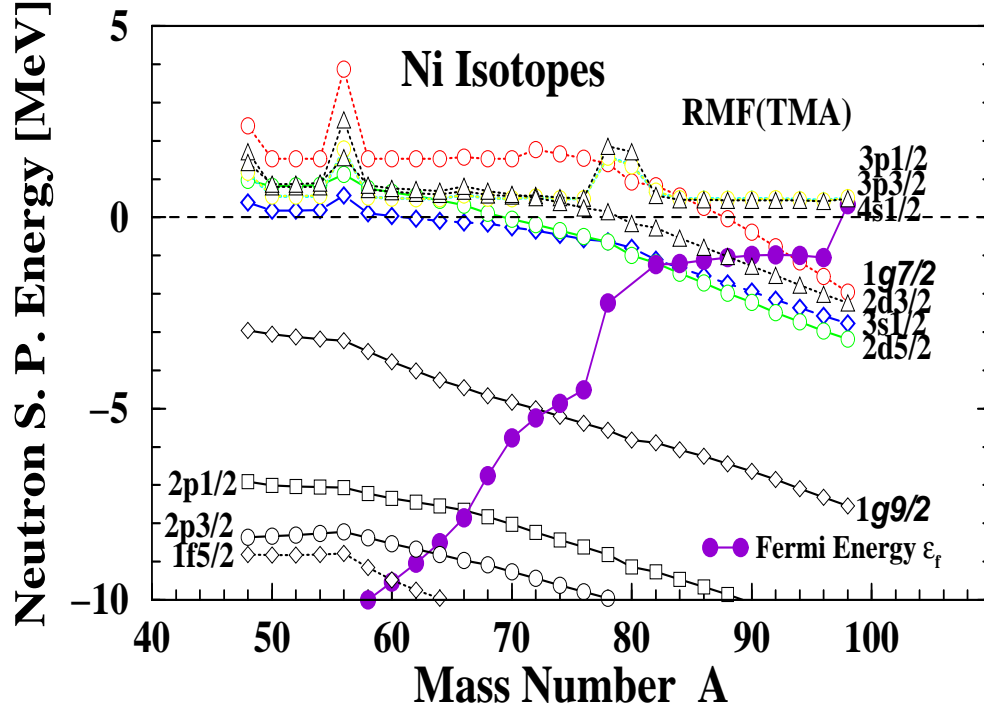


**Fig. 17.** Variation of the neutron single particle energies for the Ni isotopes with increasing mass number  $A$ . The Fermi level has been indicated by solid circles.

A detailed study of the proton, neutron and matter rms radii has also been carried out. Our RMF+BCS results for the proton and neutron rms radii and their comparison with the RCHB calculations have been displayed in fig. 18. The results obtained with the TMA and NL-SH force parameters are clearly seen to be very similar to each other. The RMF+BCS results obtained by using the NL-SH force and those of the RCHB approach using the same force are also quite close to each other as can be seen in the figure.

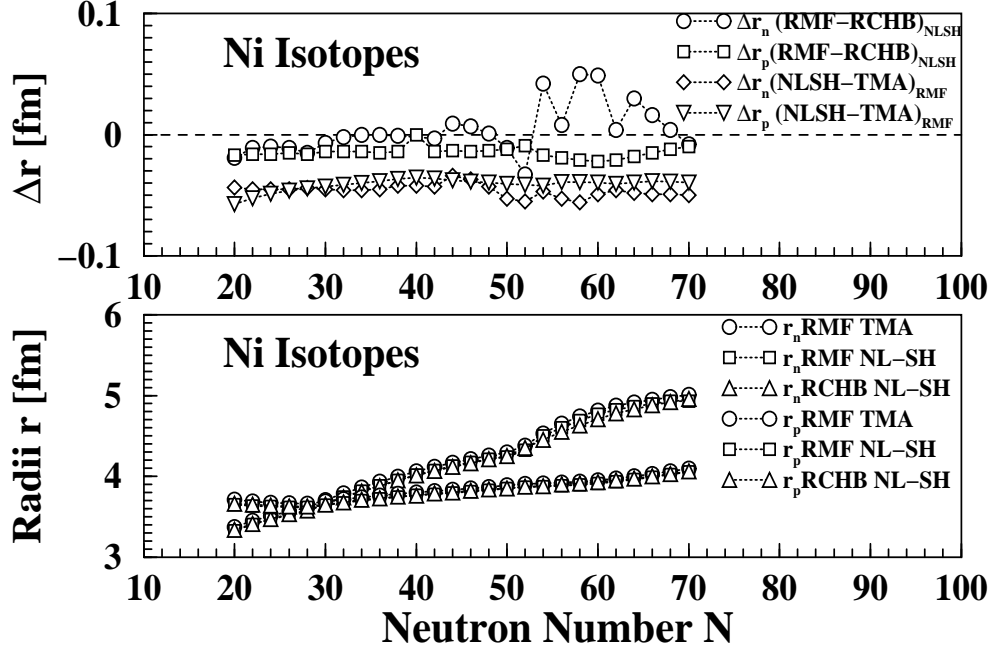


**Fig. 18.** The lower panel presents the RMF results for the proton and neutron rms radii ( $r_p$  and  $r_n$ ) for the  $^{48-98}\text{Ni}$  isotopes obtained with the TMA (open circles) and the NL-SH (open squares) force parameters. These are compared with the continuum relativistic Hartree-Bogoliubov (RCHB) calculations of Ref. 26 carried out with the NL-SH force (open triangles). The upper panel displays the difference between the our RMF, and the RCHB results of Ref. 26 for the proton and the neutron rms radii obtained for the NL-SH force. This panel also shows the difference between the calculated results for the TMA and NL-SH forces within the RMF+BCS approach.

Further, the RMF+BCS results for the rms proton radii and the neutron radii are found to be in close agreement with the available experimental data. The experimental data on the neutron and proton rms radii are available only for a few of the Ni isotopes. Our RMF+BCS results obtained with the TMA force have been plotted in fig. 19 with the the data on the proton rms radii of  $^{58-64}\text{Ni}$ , and that for the neutron rms radii of  $^{58,64}\text{Ni}$  explicitly. It is gratifying to note that the theoretical results are in good agreement with the measured radii.

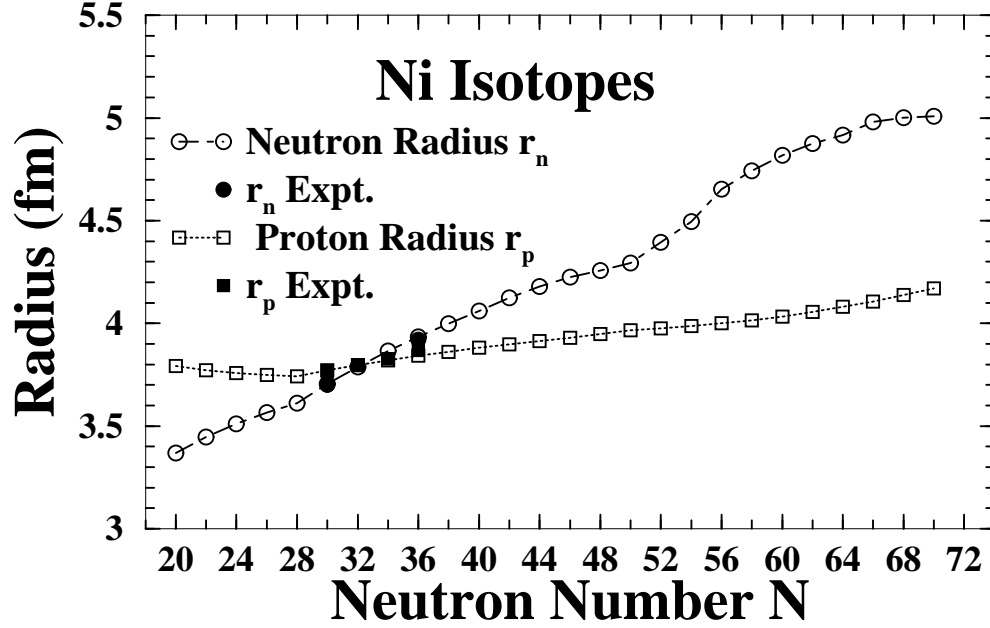


**Fig. 19.** The RMF results for the neutron,  $r_n$  (open circles) and proton,  $r_p$  (open squares) rms radii for the  $^{48-98}\text{Ni}$  isotopes obtained with the TMA force parameters. These are compared with the available experimental data shown by solid circles and solid squares for the neutron and proton radii, respectively.

The neutron skin formation is easily seen in the case of neutron rich Ni isotopes showing large spatial extension of the neutron density distributions. As a typical example, for  $^{84}\text{Ni}$  this characteristic feature is seen in Fig. 20, where we plot the density distribution for protons by hatched lines and that for the neutrons by solid line.

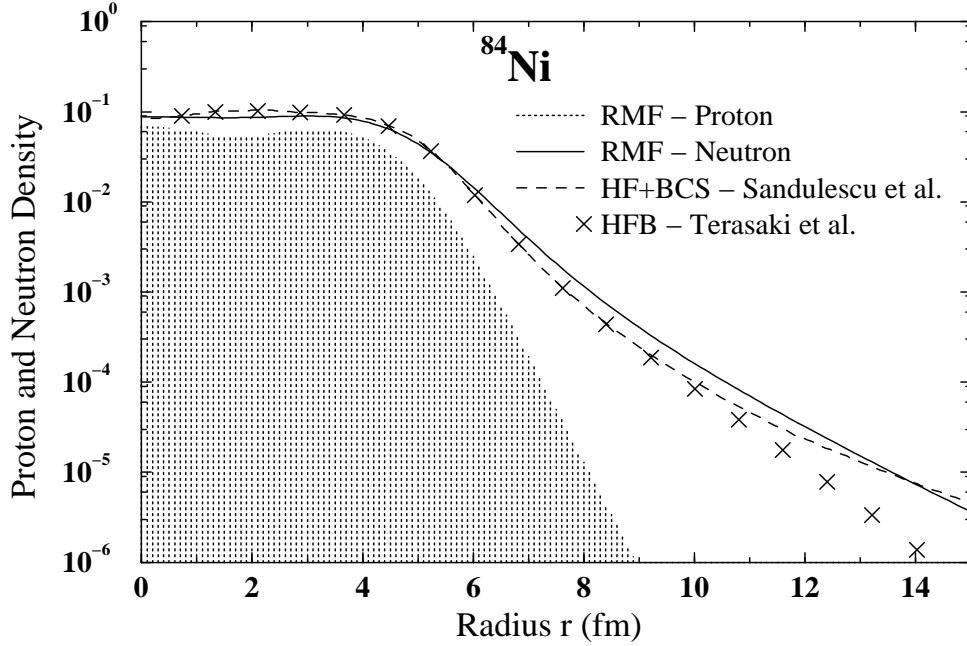


**Fig. 20.** A comparison of the neutron radial density distribution for  $^{84}\text{Ni}$  obtained in different models. The results of the present calculations shown by solid line show good agreement especially with those obtained within the resonant continuum HF+BCS approach of Ref. 6 (dashed line). The crosses correspond to the HFB results<sup>3</sup>. The radial density distribution for the protons has been shown by the hatched area.

The tail of the neutron density extends far beyond the mean field potential and has appreciable value up to about 14 fm. In order to compare our calculations with other theoretical approaches we show in fig. 20 the results of neutron density obtained using HF+BCS<sup>6</sup> and HFB<sup>3</sup> approximations. The tail of the density given by our RMF+BCS calculations is much closer to the resonant continuum HF+BCS results of Ref. 6. The main contribution to the tail of the density comes from the loosely bound states  $3s_{1/2}$  and  $2d_{3/2}$ . The fact that in the HFB calculations the tail is smaller can be due to the contribution of the pairs scattered in states which are not time reversed partners.<sup>7</sup> This contribution is not included in a BCS approach.

The neutron density distributions for the neutron rich Ni isotopes are distinct from those for the neutron rich Ca isotopes. This is clearly seen from fig. 21 which shows the neutron densities for some selected Ni isotopes. The inset in the figure displays the distribution on a logarithmic scale up to radial distance  $r = 16$  fm. A comparison of this neutron density distribution with that for the Ca isotopes displayed earlier in fig. 9 shows that in the case of neutron rich Ca isotopes we have densities with wide spatial extensions up to large distances, whereas in the neutron rich Ni isotopes it saturates. This is due to the fact that in the case of Ni isotopes the  $3s_{1/2}$  state is a bound state lying below the  $1g_{7/2}$  state which gradually

itself becomes bound while reaching towards the neutron drip line (see fig. 17). In contrast the  $3s_{1/2}$  state in the Ca isotopes remains unbound until just before the neutron drip line is reached. A partial filling in of this unbound  $3s_{1/2}$  state in the neutron rich Ca isotopes causes the formation of halos as has been discussed earlier. The single particle structures in the case of neutron rich Sn and Pb isotopes also exhibit situation similar to that in the Ni isotopes and, therefore, in these nuclei a large growth in neutron radii or halo formation is not expected to occur as one moves towards the neutron drip line.

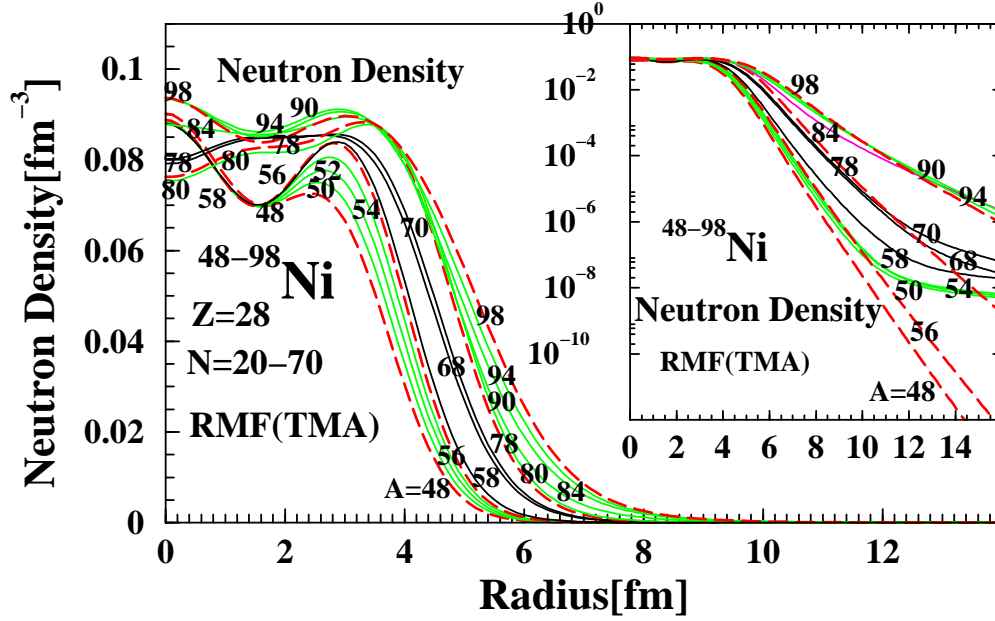


Fig. 21. Neutron radial density distribution for the  $^{48-98}\text{Ni}$  isotopes obtained in the RMF+BCS calculations using the TMA force. The dashed lines have been used to distinguish the closed neutron shell isotopes with others. The inset shows the results on a logarithmic scale up to rather large radial distances.

### 3.3. Isotopes of O, Zr, Sn and Pb Nuclei

Results for the isotopes of proton magic nuclei Sn and Pb are similar to those of proton magic Ni nuclei discussed above. The Zr nuclei are not proton magic and, therefore, there is always a contribution to the pairing energy from the protons. Also, it is found that the neutron rich Zr isotopes near the drip line have very small two neutron separation energy and constitute an example of very loosely bound system similar to the neutron rich Ca isotopes. In contrast to these nuclei, the isotopes of O show slightly different behavior as will be elaborated later. With the above mentioned similarities in view, in the following we discuss briefly the results



of O, Zr, Sn and Pb nuclei taken together in order to save space. Also, as stated earlier we restrict our treatment to spherical shapes for simplicity, even though it is likely that some of the isotopes of O and that of Zr could be actually deformed.

In fig. 22 we have displayed for some of the neutron rich representative isotopes of O, Zr, Sn and Pb nuclei the pairing gap energies of single particle states located close to the Fermi level. For our purpose we have chosen  $^{20}\text{O}$ ,  $^{138}\text{Zr}$ ,  $^{150}\text{Sn}$  and  $^{250}\text{Pb}$  to elucidate the general results for these nuclei. It is seen from fig. 22 that the pairing gaps for the single particle neutron states in the  $^{20}\text{O}$  isotope near the Fermi level range between 0.9 MeV to 1.8 MeV, where the Fermi energy lies at  $-5.22$  MeV. In contrast to Ca and Ni and other nuclei discussed here, it is seen that only the lowest neutron single particle states are occupied according to the number of neutrons, and the pairing interaction does not couple the bound states near the Fermi level with the positive energy states. Thus in the case of neutron rich O isotopes the positive energy states are not populated. It is found from our calculations that the isotopes  $^{14}\text{O}$ ,  $^{16}\text{O}$ ,  $^{22}\text{O}$ ,  $^{24}\text{O}$  and  $^{28}\text{O}$  are doubly magic. And as expected the total pairing energy for these isotopes is zero as can be seen from fig. 23.

In the case of neutron rich Zr isotopes, the single particle state  $1h_{9/2}$  is found to be a resonant state. This state has large pairing gap energy akin to that of bound states. As a representative case of the neutron rich Zr isotopes, we have plotted in fig. 22 the pairing gaps for the nucleus  $^{138}\text{Zr}$ . In this plot only the neutron states lying near the Fermi surface have been considered. The low lying resonant state at  $\epsilon = 0.6$  MeV shown in the plot is found to play an important role. The other important neutron single particle states near the Fermi level ( $\epsilon_f = -0.09$  MeV) shown in the plot are  $2f_{7/2}$ ,  $3p_{3/2}$ ,  $3p_{1/2}$ ,  $2f_{5/2}$  and  $4s_{1/2}$ . For all these states the pairing gap energy  $\Delta_j$  varies between about 0.5 MeV and 1 MeV. These gap energies are consistent with other mean field calculations and the experiments. It is further found that the high lying state  $2i_{13/2}$  at  $\epsilon = 4.13$  MeV is also a resonant state, though its contribution to the pairing energy is insignificant as it lies far above the Fermi level.

Similarly the important resonant state in the case of neutron rich Sn nuclei is found to be the neutron  $1i_{13/2}$  state. As a representative example of Sn isotopes we have plotted in fig. 22 the pairing gaps for the neutron rich  $^{150}\text{Sn}$  isotope. For this nucleus the  $1i_{13/2}$  state lies at  $\epsilon = -1.59$  MeV, whereas the Fermi energy is seen to be at  $\epsilon_f = 0.35$  MeV. Some of the important neutron single particle states near the Fermi surface for the neutron rich nucleus  $^{150}\text{Sn}$ , include the positive energy states  $4s_{1/2}$  at  $\epsilon = 0.59$  MeV, the resonant state  $1i_{13/2}$  at  $\epsilon = 0.35$  MeV, and the negative energy bound states  $2f_{5/2}$  at  $\epsilon = -0.90$  MeV. As is observed from Fig. 22, the pairing gap energy of the resonant  $1i_{13/2}$  state has a value  $\Delta_{13/2} \approx 1.5$  MeV, which is close to that of bound states like  $1h_{9/2}$ ,  $1h_{11/2}$  and  $2d_{3/2}$  etc. The other state in the continuum which has somewhat appreciable gap energy is the  $2g_{9/2}$  state at around 2 MeV. However, this state being higher in energy as compared to the Fermi energy, plays only a minor role in the contribution to the total pairing energy of the nucleus.

The gap energies for the single particle states shown in fig. 22 are found to be consistent with the results obtained from the HFB and RHB calculations<sup>4,20,30</sup>.

To elaborate, the HFB+D1S results of Lalazissis et al.<sup>4</sup> for the pairing gaps  $\Delta_{nlj}$  in the nucleus  $^{150}\text{Sn}$  for the deep bound states are about 2 MeV, while those for states near the Fermi surface are about 1.75 MeV, and those for the high lying continuum states it decreases from about 1.5 MeV to about 0.5 MeV. In contrast, the HFB+SKP results yield gaps ranging from very small values of about 0.5 MeV for deep hole states, to about 1.5 MeV for the states near the Fermi level, to about 0.75 MeV for the high lying particle states in the continuum. Further, the HFB+SKP <sup>$\delta$</sup>  calculations provide results wherein the gaps for the states throughout have almost a constant value of about 1.2 MeV with a small variation of about  $\pm 0.2$  MeV. A comparison of these results with our RMF+BCS calculations shows the closest agreement with the HFB+SKP <sup>$\delta$</sup>  calculations. As has been pointed out by Dobaczewski et al.<sup>4</sup>, the D1S interaction somewhat overestimates the gaps due to large magnitude of the strength of D1S interaction. Similarly, the detailed results published by Dobaczewski et al.<sup>4</sup> for the nucleus  $^{120}\text{Sn}$  are found to be in close agreement for the various single particle states. Indeed, the results for the average neutron gaps quoted in the calculations of Dobaczewski et al.<sup>4</sup> using the SKP <sup>$\delta$</sup>  interaction for the entire chain of Sn nuclei up to neutron number  $N=126$ , which represents the neutron drip line, are found to be consistent with our RMF+BCS calculations.

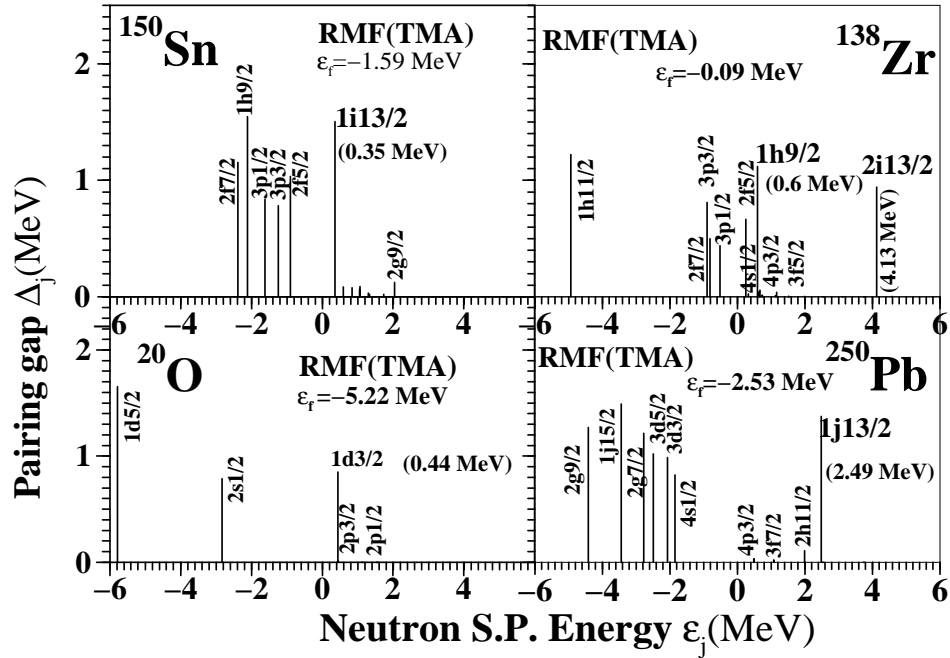


**Fig. 22.** Pairing gap energy  $\Delta_j$  of neutron single particle states with energy close to the Fermi surface for the neutron rich nuclei  $^{20}\text{O}$ ,  $^{138}\text{Zr}$ ,  $^{150}\text{Sn}$  and  $^{250}\text{Pb}$ .

Finally, fig. 22 also shows a similar plot for the nucleus  $^{250}\text{pb}$  representing the neutron rich case of the Pb isotopes. The neutron state  $1j_{13/2}$  shown in the plot at

energy  $\epsilon = 2.48$  MeV is a resonant state. As is seen from the plot this state has large pairing gap,  $\Delta_j \approx 1.5$  MeV comparable to the bound single particle states  $3d_{5/2}$ ,  $3d_{3/2}$  etc. near the Fermi level. The pairing gaps values for the Pb isotopes are found to be consistent with those obtained in other mean field calculations<sup>20,30,4,32</sup>.

### 3.3.1. Pairing Energy

Apart from the case of Zr isotopes, O, Ca, Ni, Sn and Pb nuclei considered here are all proton magic and, therefore, for these nuclei the contribution to total pairing energy is mostly from the neutron single particle states. Thus for the proton magic nuclei, the pairing energy vanishes for  $N$  values corresponding to the neutron shell closures. This can be seen in fig. 23 which displays the total pairing energy contribution for the nuclei O, Zr, Sn and Pb as a function of neutron number  $N$ .

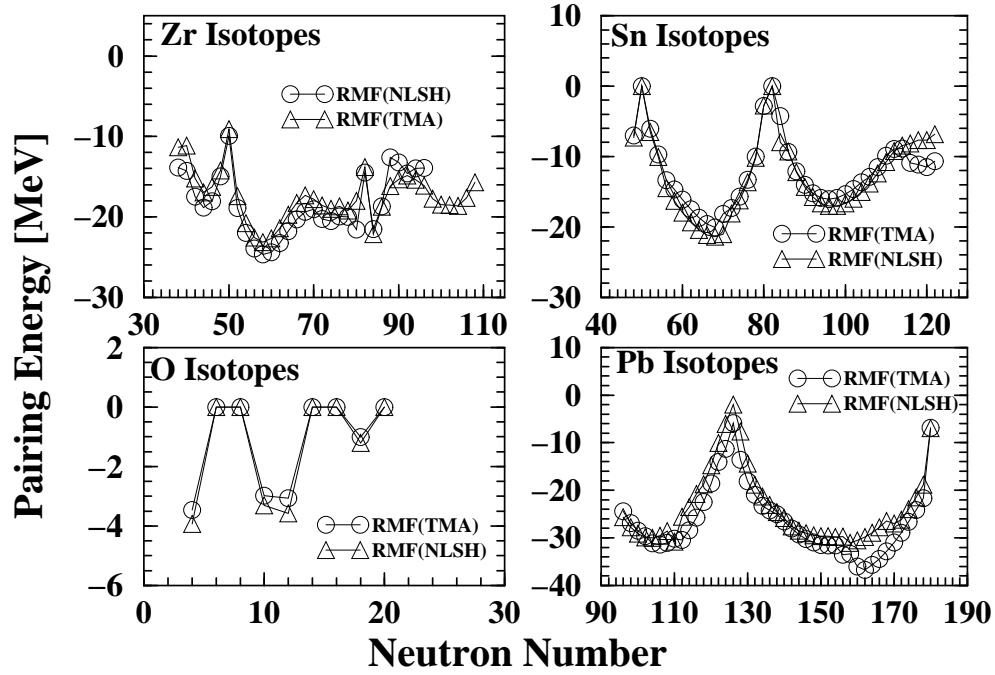


**Fig. 23.** Present RMF results for the pairing energy for the O, Zr, Sn and Pb isotopes obtained with the TMA (open squares) are compared with those obtained using the NL-SH (open triangles) force parameters.

It is seen from the plot for the O isotopes in fig. 23 that the neutron shell closures for O isotopes occur for  $N=6, 8, 14, 16$  and  $20$ . Similarly, for the Sn isotope it is observed to occur for  $N=50$  and  $82$ , whereas in the case of Pb isotopes  $N=126$  is found to correspond to the neutron shell closure. However, some neutron rich isotopes of Sn and Pb, due to reorganization of single particle states, do not continue to be proton magic and, hence, there are contributions to the total pairing energy from proton single particle states as well. In contrast, Zr is not a proton

magic nucleus. Thus, as such both the proton and neutron single particle states contribute to the total pairing energy. Therefore one observes slightly different feature of the  $N$  dependence of the pairing energy as compared to that of the proton magic nuclei. This can be seen from the plot for the Zr isotopes in fig. 23. The figure shows that for  $N = 50$  and  $N = 82$  the total pairing energy is close to 10 MeV and 15 MeV, respectively, and it is solely due to the protons. Similarly, for  $N = 40$  and  $N = 70$  due to sub-shell behavior of the isotopes, the pairing energy is reduced. Midway between  $N = 50$  and  $N = 70$ , it is found to be maximum as expected.

Further, from the plot of the Sn isotopes in fig. 23, it is seen that the pairing energy vanishes for  $N = 50$  and  $N = 82$  due to shell closure. The maximum pairing energy values are found to occur for isotopes in the midway between the neutron magic numbers 50 and 82. Similar behaviour for the  $N$  dependence of the pairing energy is approximately seen for isotopes lying between the magic numbers  $N = 82$  and  $N = 126$ . For large neutron number approaching  $N = 126$  it is found that the proton single particle states are reorganized such that the Sn isotopes are no more proton magic and, therefore, there is finite contribution from the protons to the total pairing energy. This makes the shape of the curve for the pairing energy for  $N > 112$  flatter than expected while approaching the neutron magic number  $N = 126$ . The pairing energy values obtained in our RMF+BCS calculations are found to be of similar magnitude as those obtained in other mean field calculations<sup>20,4,32</sup>. Further from fig 23 it is seen that the results obtained using the TMA and NL-SH forces are very close to each other. However, slight differences occur in some of the Sn and Pb isotopes with large neutron numbers.

### 3.3.2. *Two Neutron Separation Energy*

In the lower panel of Fig. 24 we have shown the two neutron separation energy  $S_{2n}$  for the O isotopes. Further, the results of RMF+BCS calculations employing the TMA<sup>17</sup> and the NL-SH<sup>27</sup> forces have also been shown along with those obtained in the RCHB approach for the purpose of comparison.

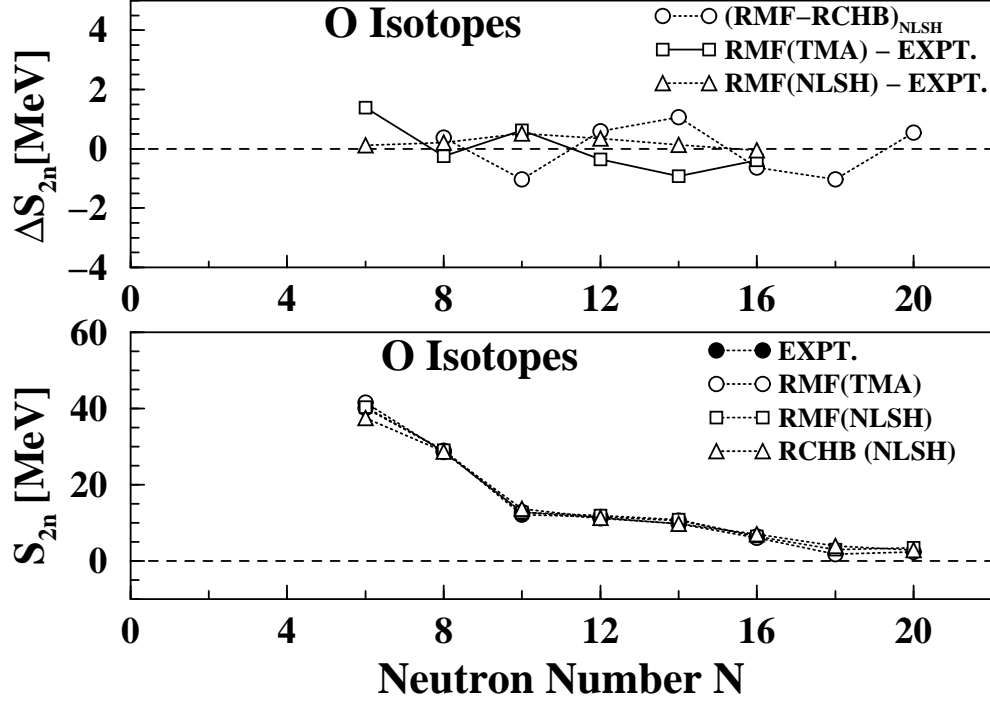


**Fig. 24.** In the lower panel the present RMF results for the two neutron separation energy for the  $^{12-28}\text{O}$  isotopes obtained with the TMA (open circles) and the NL-SH (open squares) force parameters are compared with the continuum relativistic Hartree-Bogoliubov (RCHB) calculations of Ref. 26 carried out with the NL-SH force (open triangles) for the purpose of comparison. The lower panel also depicts the available experimental data<sup>25</sup> (solid circles) for the purpose of comparison. The upper panel depicts the difference in the RMF+BCS results and the RCHB results of Ref. 26 for the two neutron separation energy obtained for the NL-SH force. This plot also shows the difference of the calculated results with respect to the available experimental data<sup>25</sup>.

It is seen from the figure that the calculations using two different force parameters, the TMA and the NL-SH Lagrangian, yield almost similar results as in the case of Ca and Ni isotopes described earlier. Also, it is observed that the results for the NL-SH force using the RCHB approach and the present RMF+BCS calculations are quite close to each other. The upper panel depicts the difference between the results obtained using the RMF+BCS and the RCHB approaches. The difference is indeed small, a maximum difference is seen for  $^{18}\text{O}$  and it is less than 1 MeV. It is further seen that the calculated results for  $S_{2n}$  are in good agreement with the experimental data. The upper panel depicts the difference between the experimental and calculated values. The maximum difference is about 1.5 MeV. The calculated two neutron drip line is found to occur at  $N = 20$  in both the RMF+BCS and the

RCHB calculations. However, in contrast it is experimentally<sup>35</sup> observed to occur at  $N = 16$ . The discrepancy between the theoretical prediction and the experimental data is found almost in all the mean field calculations employing both relativistic as well as non-relativistic approaches.

A better insight into the position of the neutron drip line can be gained by looking at the dependence of the neutron single particle states around the Fermi level as a function of increasing neutron number  $N$ . This has been shown in fig. 25 for the bound neutron  $1d_{5/2}$ ,  $2s_{1/2}$  and  $1d_{3/2}$  states, as well as for the unoccupied  $2p_{3/2}$ ,  $2p_{1/2}$  and  $1f_{7/2}$  states lying in the continuum.

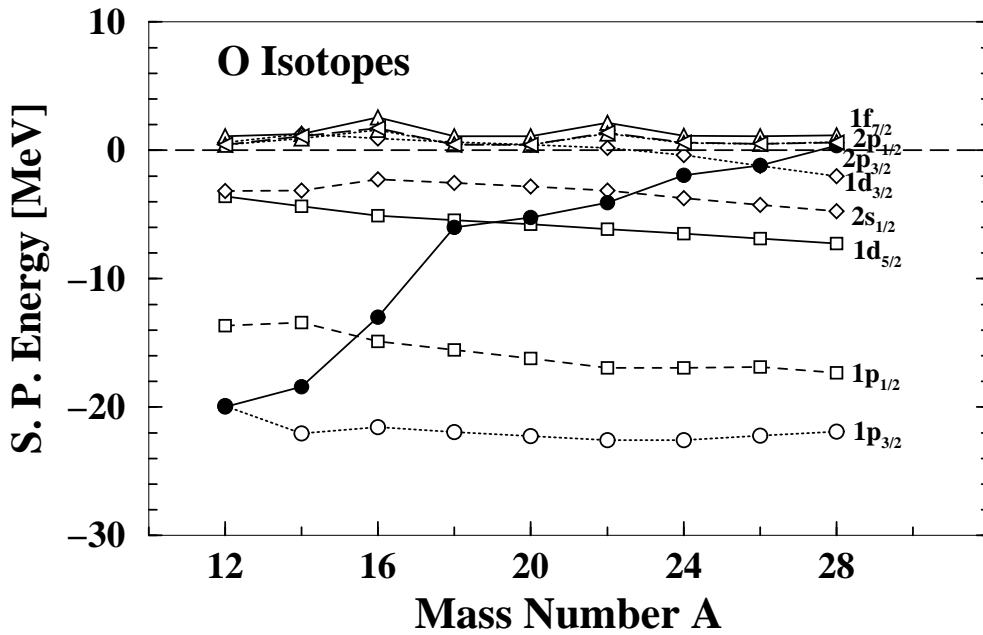


**Fig. 25.** Variation of the neutron single particle energies for the O isotopes with increasing mass number A.

It is seen from fig. 25 that with increasing neutron number  $N$ , the bound states near the Fermi level, for example,  $1d_{3/2}$  and  $2s_{1/2}$  etc. have a tendency to come down in energy. For  $N \leq 14$  the crucial  $1d_{3/2}$  state remains unbound and lies close to other unbound states  $2p_{3/2}$ ,  $2p_{1/2}$ , and  $1f_{7/2}$ , while the neutron Fermi energy increases with increasing neutron number  $N$ . Around  $N = 16$ , the  $1d_{3/2}$  state comes down to become bound, whereas the other neighboring states  $2p_{3/2}$ ,  $2p_{1/2}$ ,  $1f_{7/2}$  and  $1g_{9/2}$  continue to remain unbound. With further addition of two neutrons, at  $N = 18$ , the  $1d_{3/2}$  state becomes even more bound while the neutron Fermi energy approaches to zero. For  $N = 20$ , the Fermi energy becomes positive and the  $1d_{3/2}$  state is fully occupied. This results in a stable  $^{28}\text{O}$  isotope, the heaviest one. Beyond this the neutron Fermi energy becomes positive and any further addition

of neutrons makes the isotope unstable. Thus the essential point for the position of the neutron drip line is that beyond  $A = 24$ , the  $1d_{3/2}$  orbital is slightly too bound and that the continuum states  $2p_{3/2}$ ,  $2p_{1/2}$ ,  $1f_{7/2}$  and  $1g_{9/2}$ , though close to zero energy, remain entirely unoccupied. As shown in fig. 26, a study of  $N$  dependence of the spin-orbit splitting energy  $E_{ls} = (E_{nlj=l-1/2} - E_{nlj=l+1/2})/(2l+1)$  of the spin-orbit doublet  $1d_{3/2}$  and  $1d_{5/2}$  indicates that the neutron doublet splitting energy is slightly reduced beyond  $A = 24$  and, therefore, the  $1d_{3/2}$  orbital is pushed down and accommodates further addition of 4 neutrons.

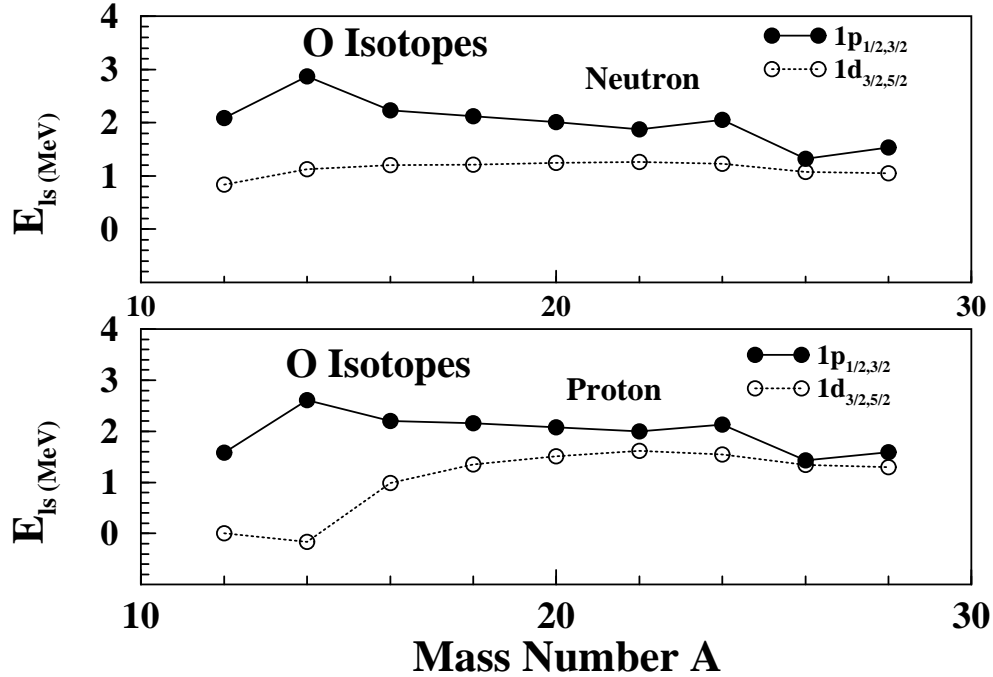


**Fig. 26.** Variation of the spin-orbit splitting energy  $E_{ls}$  for the neutron (upper panel) and proton (lower panel) doublets ( $1p_{1/2}, 1p_{3/2}$ ) and ( $1d_{3/2}, 1d_{5/2}$ ) in the O isotopes with increasing mass number  $A$ .

From the above discussion it appears that for the neutron rich O, the pairing interaction beyond  $A = 24$  is not strong enough to populate the positive energy states near the Fermi level, for example,  $2p_{3/2}$ ,  $2p_{1/2}$  and  $1f_{7/2}$  etc., to make the isotopes heavier than  $A = 24$  unstable. This discrepancy between the theoretical results and the measurements for the two neutron drip line in the O isotopes is found in most of the mean field calculations<sup>4,20,30,32,36</sup> and needs further investigations.

Next we consider the Zr isotopes for which the two neutron separation energies have been plotted in the lower panel of fig. 27, whereas the upper panel shows the differences between the  $S_{2n}$  values obtained from theoretical predictions and the

measurements. It is seen from fig. 27 that the degree of agreement between the available experimental data and the theoretical results using TMA and NLSH force parameterizations are of similar quality as for the isotopes of other nuclei discussed earlier. In this case the maximum difference between the measured  $S_{2n}$  and the predicted value for it is found to occur for a few isotopes around  $N = 54$ , and is less than 3 MeV. Again, as for the results of other nuclei and their isotopes, the RCHB and the RMF+BCS calculations for the Zr isotopes are also found to be in excellent agreement with each other as is evident from fig. 27. With regard to the discrepancy around  $N = 54$  between the data and the results obtained in the RMF+BCS as well as in the RCHB calculations, it may be pertinent to remark that the present calculations treat these nuclei as spherical whereas actually some of the Zr isotopes are believed to be well deformed. Whether an inclusion of deformation in the present RMF+BCS approach would markedly improve the calculated results needs further investigations.

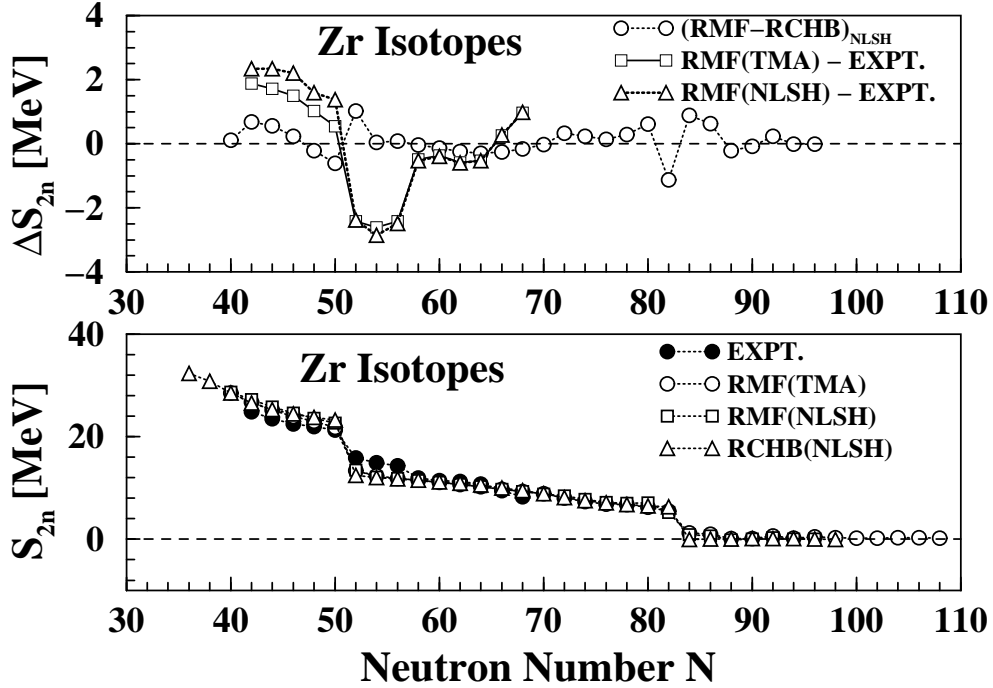


**Fig. 27.** The present RMF results for the two neutron separation energy for the Zr isotopes obtained with the TMA (open circles) and the NL-SH (open squares) force parameters are compared with the continuum relativistic Hartree-Bogoliubov (RCHB) calculations of Ref. 26 carried out with the NL-SH force (open triangles), and with the available experimental data<sup>25</sup> (solid circles). The upper panel depicts the difference in the RMF+BCS results and the RCHB results of Ref. 26 obtained for the NL-SH force along with the difference of the calculated results with respect to the available experimental



data<sup>25</sup>.

The calculations employing the NL-SH force for the mean field description predict the heaviest stable isotope to be  $^{136}\text{Zr}$ . This is true for both the RMF+BCS as well as the RCHB calculations as can be seen from fig. 27. The results obtained using the TMA force are at variance with this prediction and the two neutron drip line is found to occur at  $N = 112$  corresponding to  $^{152}\text{Zr}$  isotope. This difference in the predictions of the two neutron drip line is due to the dissimilarities in the spectrum of single particle states near the neutron Fermi level. Further, it is seen from fig. 27 that the  $S_{2n}$  values for  $N \geq 84$  is rather small, and is reduced further more with increasing number of neutrons. For neutron numbers around  $N \geq 84$  the  $S_{2n}$  values are close to a few hundred keV. Such a physical situation for very loosely bound systems has already been seen to occur for highly neutron rich Ca isotopes.

In order to have a better understanding of such loosely bound extremely neutron rich  $^{124-152}\text{Zr}$  isotopes, we have shown in fig. 28 the variation of neutron single particle energy for the states near the Fermi level obtained with the TMA force.

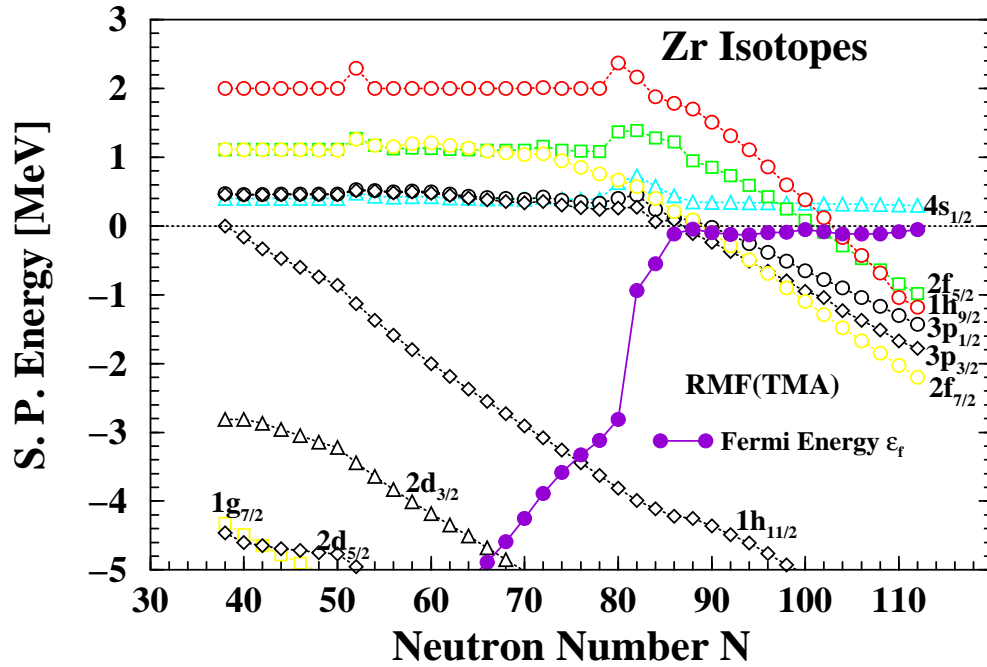


**Fig. 28.** Variation of the neutron single particle energies for the Zr isotopes with increasing neutron number  $N$  for the TMA force.

It is seen from fig. 28 that for these neutron rich Zr isotopes the neutron Fermi

level lies almost at zero energy. The important neutron single particle states with finite occupancy near the Fermi level are  $1h_{9/2}$ ,  $2f_{5/2}$ ,  $2f_{7/2}$ ,  $3p_{1/2}$ ,  $3p_{3/2}$  and  $4s_{1/2}$ . For  $N = 82$  corresponding to  $^{122}\text{Zr}$ , we have shell closure for the neutron states. For this nucleus the neutron states up to  $1h_{11/2}$  are completely filled and the higher states are completely empty as is expected of a closed shell system. On further addition of two neutrons, the occupation pattern of states gets changed as compared to that of  $^{122}\text{Zr}$  nucleus in the sense that the added neutrons simply do not occupy the next higher state. Instead the neutrons are redistributed amongst the  $1h_{11/2}$  and the states  $3p_{3/2}$ ,  $2f_{7/2}$ ,  $3p_{1/2}$ ,  $2f_{5/2}$ ,  $1h_{9/2}$  and the high lying resonant state  $1i_{13/2}$ . Also as we keep adding more and more neutrons the positive energy states  $3p_{3/2}$ ,  $2f_{7/2}$ ,  $3p_{1/2}$ ,  $2f_{5/2}$  and  $1h_{9/2}$  gradually come down in energy and subsequently become bound for larger neutron number  $N$  as is seen in fig. 28. To illustrate this we consider the detailed single particle structure of, for example,  $^{126}\text{Zr}$  and  $^{138}\text{Zr}$  nuclei. For the nucleus  $^{126}\text{Zr}$  the occupation weight of the state  $3p_{3/2}$  at energy  $\epsilon = 0.05$  MeV is 0.33, of  $2f_{7/2}$  at energy  $\epsilon = 0.22$  MeV is 0.27, of  $3p_{1/2}$  at energy  $\epsilon = 0.28$  MeV is 0.10, of  $2f_{5/2}$  at energy  $\epsilon = 1.20$  MeV is 0.03, of  $1h_{9/2}$  at energy  $\epsilon = 1.82$  MeV is 0.03, and that of the high lying resonant state  $1i_{13/2}$  at energy  $\epsilon = 5.14$  MeV is 0.03. All these positive energy states accommodate together about 4.5 neutrons. However, the first three of these states lying very close to the Fermi level ( $\epsilon_f = -0.06$  MeV) have the major share of about 3.6 neutrons. In comparison consider the nucleus  $^{138}\text{Zr}$  which is reached after an addition of 12 neutrons to the nucleus  $^{126}\text{Zr}$ . Due to the additional neutrons, the  $2f_{7/2}$ ,  $3p_{3/2}$  and  $3p_{1/2}$  states become bound whereby  $2f_{7/2}$  state becomes lower in energy as compared to that of  $3p_{3/2}$ . Also, the neutron Fermi energy is slightly changed to  $\epsilon_f = -0.09$  MeV. Now the occupation weight of the state  $2f_{7/2}$  at energy  $\epsilon = -0.90$  MeV is 0.85, of  $3p_{3/2}$  at energy  $\epsilon = -0.81$  MeV is 0.90, of  $3p_{1/2}$  at energy  $\epsilon = -0.51$  MeV is 0.84, of  $2f_{5/2}$  at energy  $\epsilon = 0.25$  MeV is 0.27, of  $1h_{9/2}$  at energy  $\epsilon = 0.60$  MeV is 0.24, and that of another high lying resonant state  $2i_{13/2}$  at energy  $\epsilon = 4.13$  MeV is 0.01. In this case the positive energy states accommodate together about 4 neutrons. On further addition of neutrons, the positive energy states  $2f_{5/2}$  and  $1h_{9/2}$  also gradually become bound and thus can accommodate neutrons up to  $N = 112$  which correspond to a shell closure. Thus one is able to reach a bound  $^{152}\text{Zr}$  nucleus. It is remarkable that the energy of the neutron  $4s_{1/2}$  single particle state remains positive and almost constant with increasing neutron number beyond  $N = 90$  as is seen from fig. 28. And, therefore, further increase of neutrons which fill in the next available  $4s_{1/2}$  state make the nucleus  $^{154}\text{Zr}$  unbound. Further, due to the fact that for the neutron rich ( $N = 84$  to  $N = 90$ )  $^{124-130}\text{Zr}$  isotopes, one of the last partially occupied states is the positive energy  $3p_{1/2}$  state having low orbital angular momentum and a reduced centrifugal barrier, the density distribution of these exotic nuclei assumes a wider extension. It is in turn reflected in neutron radii becoming rather large as can be seen in fig. 33. This may give rise to halo formation as in the case of Ca isotopes discussed earlier. However, it should be emphasized that the case of neutron rich Zr isotopes is slightly different. In the case of Ca isotopes, one of the outermost positive energy single particle states which is partially occupied is the  $3s_{1/2}$  state. This state with orbital angular momentum  $l = 0$  and having no centrifugal barrier provides a more favorable condition for a halo formation,

as compared to the  $3p_{1/2}$  state in the neutron rich Zr isotopes. Beyond  $^{130}\text{Zr}$  the neutron  $3p_{1/2}$  state becomes bound and the positive energy resonant states  $2f_{5/2}$  and  $1h_{9/2}$  continue together to accommodate more neutrons. As the nucleus  $^{142}\text{Zr}$  is reached, the  $2f_{5/2}$  becomes bound. On further addition of two neutrons the  $1h_{9/2}$  state also becomes bound and continues to accommodate more neutrons until completely filled. For the  $^{144-152}\text{Zr}$  isotopes the occupation weights of the positive energy states like  $4p_{3/2}$  and  $4p_{1/2}$  located close to the continuum threshold remains almost negligible.

The single particle structure obtained with increasing neutron number in the case of RMF+BCS calculations carried out with the NL-SH force is slightly at variance with that seen above for the TMA force. In this case one observes that the neutron states  $3p_{3/2}$ ,  $2f_{7/2}$ , and  $3p_{1/2}$  as for the TMA results gradually become bound with increasing neutron number. However, the states  $2f_{5/2}$  and  $1h_{9/2}$  do not come down sufficiently in energy and, thus, remain positive energy states as has been shown in the lower panel of fig. 29. Consequently, with the NL-SH force one has the nucleus  $^{136}\text{Zr}$  as the heaviest bound system. In order to gain more insight into the role of resonant and other states near the Fermi level in accommodating more and more neutrons to have extremely neutron rich isotopes, we have shown in the upper panel of fig. 29 the occupancy in terms of number of neutrons occupying the above mentioned crucial states  $1h_{9/2}$ ,  $2f_{5/2}$ ,  $3p_{3/2}$ ,  $2f_{7/2}$ , and  $3p_{1/2}$ . As is seen in this part of the figure, all these states at the threshold of the continuum are partially occupied for  $N = 84$  ( $^{124}\text{Zr}$ ). The total number of nucleons occupying these positive energy states is about two, approximately one each in the  $2f_{5/2}$  and  $1h_{9/2}$  states. The occupancy of other states is almost negligible. We note that the neutron states  $3p_{3/2}$ ,  $2f_{7/2}$ , and  $3p_{1/2}$  are hardly bound. With addition of two neutrons at  $N = 86$  ( $^{126}\text{Zr}$ ) all the states come down in energy. Now there are more than three neutrons in the positive energy states, mainly the states  $3p_{3/2}$  and  $2f_{7/2}$  are occupied with one and two neutrons, respectively. With further addition of two neutrons at  $N = 88$  ( $^{128}\text{Zr}$ ), the  $3p_{3/2}$  state becomes bound, and the  $3p_{1/2}$  and  $2f_{7/2}$  states are now hardly bound. For this case the number of neutrons in the continuum is now less than three occupying the  $3p_{1/2}$  and  $2f_{7/2}$  states. In a similar manner for  $N = 90$  ( $^{130}\text{Zr}$ ) it is seen from the figure that the state  $2f_{7/2}$  also becomes just a bound one and there are about a little more than one neutron in the continuum, mostly in the  $3p_{1/2}$  state. Finally for  $N = 92$  corresponding to ( $^{132}\text{Zr}$ ) the  $3p_{3/2}$ ,  $2f_{7/2}$ , and  $3p_{1/2}$  become bound states and the states  $2f_{5/2}$  and  $1h_{9/2}$  continue to remain unbound. It is seen from the figure that for the isotopes ( $^{132-136}\text{Zr}$ ) the number of nucleons occupying the continuum states is less than one. From these considerations one clearly sees the important role of resonant states and that of loosely bound states like  $1h_{9/2}$ ,  $2f_{5/2}$ ,  $3p_{3/2}$ ,  $2f_{7/2}$ , and  $3p_{1/2}$  in accommodating more and more nucleons to produce exotic neutron rich loosely bound isotopes of ( $^{124-136}\text{Zr}$ ).

Further, on the other hand, the single particle state  $4s_{1/2}$  is found to exhibit similar behavior of variation for both the TMA and NL-SH forces and with addition of neutrons it remains throughout an unbound state without significant occupancy. This prohibits the very heavy neutron rich isotopes of Zr to exhibit as prominent halo formation as predicted for the heavy neutron rich Ca isotopes.

Also, it should be emphasized that the difference in the binding energy of the loosely bound  $^{132-152}\text{Zr}$  isotopes obtained in the case of TMA force is in fact very small, of the order of 100 keV for the neighboring two isotopes. With this in view, the difference in the positions of the two-neutron drip line as predicted for the TMA and NL-SH forces should not be treated too seriously.

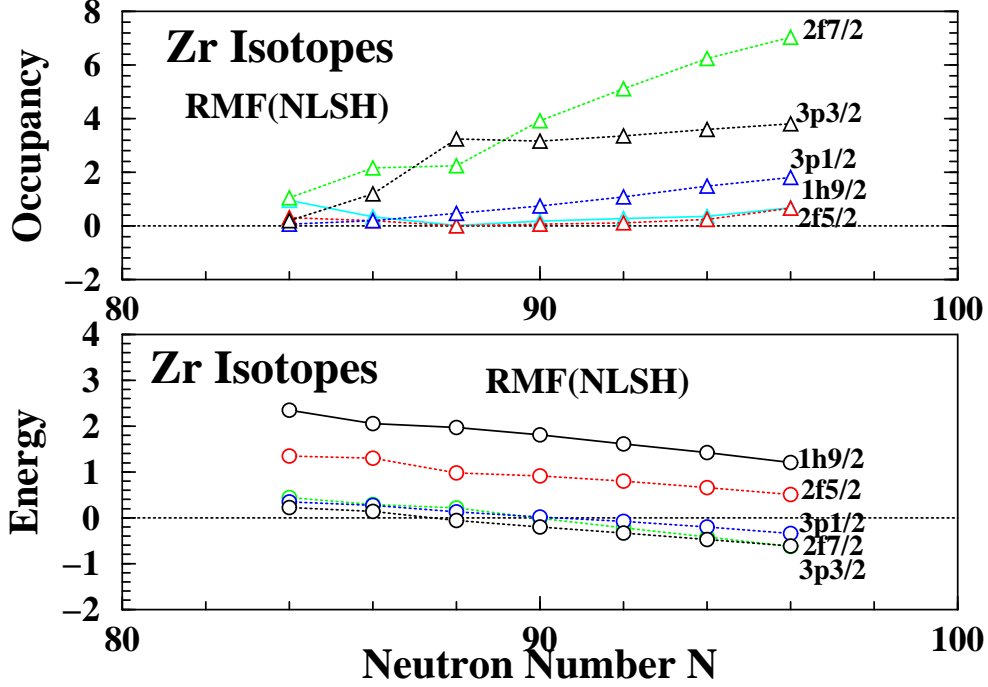


**Fig. 29.** Lower Panel: Variation in energy of the neutron single particle states for the  $^{124-136}\text{Zr}$  isotopes with increasing neutron number  $N$  for the NL-SH force. Upper Panel: Occupancy of the single particle states in terms of number of neutrons with increasing neutron number.

In Fig. 30 we have displayed results of the two neutron separation energy  $S_{2n}$  for the Sn isotopes. The difference between the RCHB and the RMF+BCS results have been shown in the upper panel of the figure. It is indeed small for most of the isotopes. The maximum difference between the two approaches, which occurs in a few case is approximately 1 MeV. Similarly a comparison with the available experimental data shows that both the TMA and NL-SH forces provide a good description of the two neutron separation energies. However, the maximum difference of approximately 2 MeV is found for a few Sn isotopes as can be seen in the upper panel of fig. 30. It is found that the RMF+BCS calculations using either TMA or NL-SH forces predict  $^{176}\text{Sn}$  to be the heaviest stable isotope. In complete agreement, the RCHB calculations also predict the two neutron drip line to occur

at  $N = 126$  corresponding to  $^{176}\text{Sn}$ .

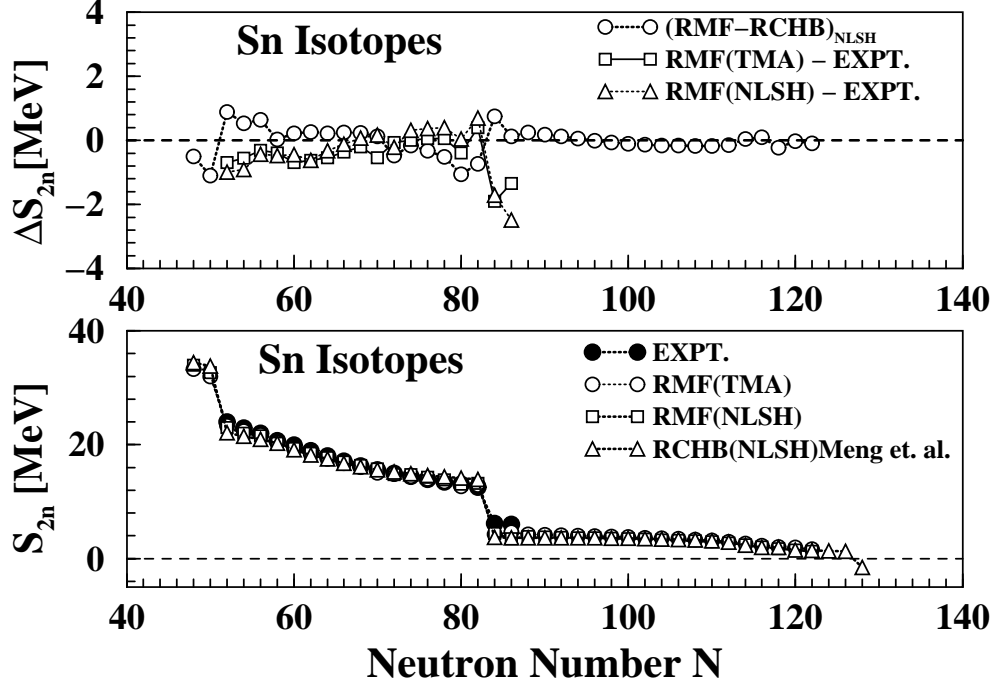


**Fig. 30.** RMF+BCS results and their comparisons with that of RCHB calculations of ref. 26, and available experimental data<sup>25</sup>  $^{104-136}\text{Sn}$  for the two neutron separation energy for the  $^{98-172}\text{Sn}$  isotopes. For details see the caption for fig. 27.

Similar results of the two neutron separation energy  $S_{2n}$  for the Pb isotopes are displayed in fig. 31. As before the upper panel shows the difference between different results plotted in the lower panel. It is to be noted that the RCHB calculations for the Pb isotopes by Meng et al.<sup>19</sup> have been reported only up to  $N = 150$  which correspond to the  $^{232}\text{Pb}$  isotope. Due to this we have shown only the limited results for the RCHB calculations in fig. 31. It is seen from the figure that the RMF+BCS results are very close to those obtained using the RCHB approach. The difference between the RCHB and the RMF+BCS results have been shown in the upper panel of the figure. It is indeed small for most of the isotopes. The maximum difference between the two approaches, which occurs in a few case is approximately 1 MeV. Similarly a comparison with the available experimental data shows that both the TMA and NL-SH forces provide an equally good description of the two neutron separation energies for the Pb isotopes. The two neutron drip line for the Pb isotopes is found to occur at  $N = 184$  corresponding to  $^{266}\text{Pb}$  isotope.

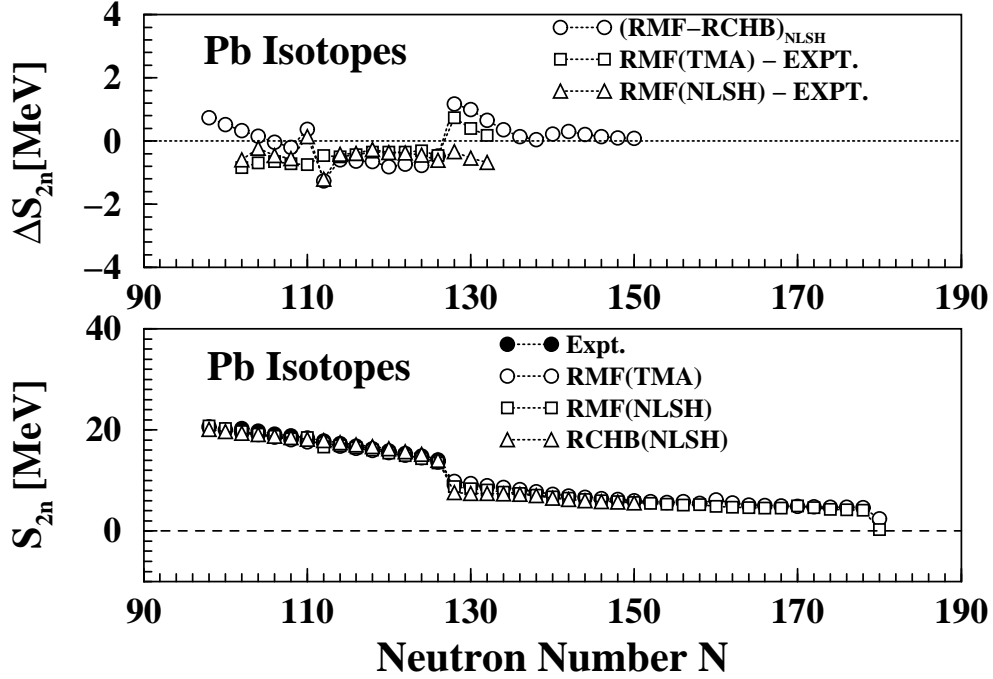


**Fig. 31.** RMF+BCS results and their comparisons with that of RCHB calculations of ref. 26, and the available experimental data<sup>25</sup> ( $^{184-214}\text{Pb}$ ) for the two neutron separation energy for the  $^{180-262}\text{Pb}$  isotopes. For details see the caption for fig. 27.

### 3.3.3. RMS Radii for Proton and Neutron Distributions

Earlier we have made a detailed comparison of RMF+BCS results with those obtained in the RCHB calculations<sup>26</sup>, and with the available experimental data for the rms radii of proton and neutron distributions for the Ca and Ni isotopes as displayed in figs. 6 and 18. Similar comparisons for the results of these rms radii for O, Zr, Sn and Pb isotopes lead us to conclude that the rms proton, neutron and matter radii as obtained in the RMF+BCS description are quantitatively in good agreement with those obtained in a more complete RCHB approach. Also, the results for these radii using the TMA and the NL-SH forces are observed to be very close to each other. Furthermore, it is found that the calculated proton and neutron rms radii are in good agreement with the available experimental data. As an illustration we have shown in fig. 32 the calculated RMF+BCS results (open triangle) obtained with the TMA force for the proton rms radii in comparison with the available measured data (open circles). The agreement with the data is indeed very satisfactory.

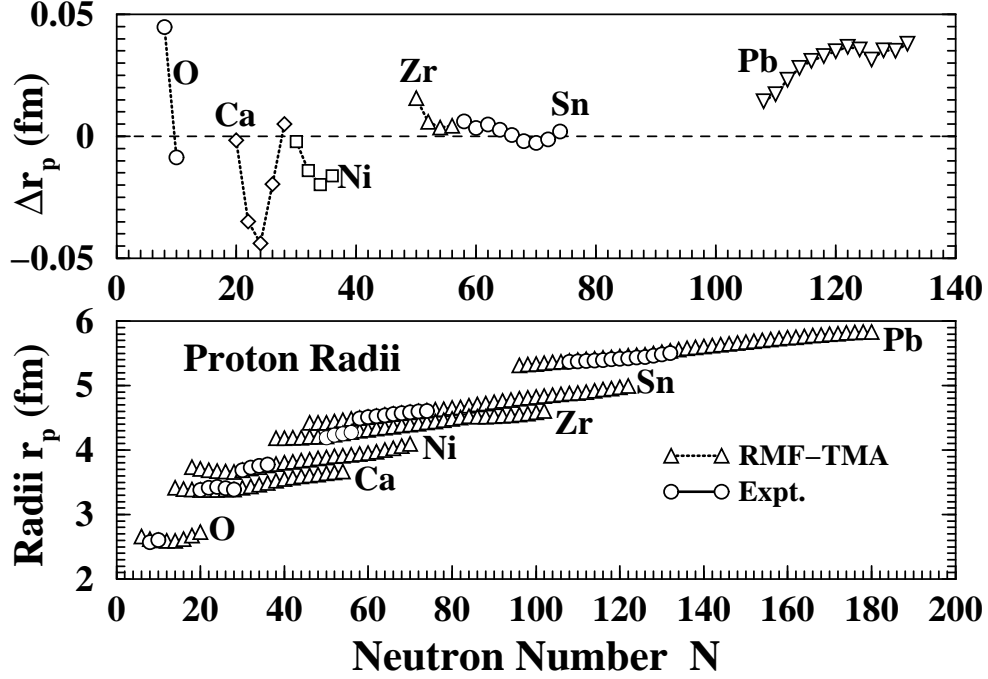


**Fig. 32.** In the lower panel present RMF results for the proton rms radii  $r_p$  for the isotopes of various nuclei obtained with the TMA force parameters are compared with the available experimental data<sup>25</sup> (open circles). The upper panel shows the difference between the measured and calculated radii for the isotopes for which data are available.

Further, in fig. 33 we have shown in various columns the theoretical predictions for the rms neutron radii. It is found that the variation of the neutron radii for the chains of isotopes of nuclei studied here only approximately follows the  $N^{1/3}$  law ( $r_n = r_0 N^{1/3}$ ) as has been shown in fig. 33. One observes deviation from the law for the case of rich proton as well as rich neutron isotopes. The figure also shows the value of radius constant  $r_0$  providing the best fit to the radii. As is seen from fig. 33, this best fit is obtained with gradually reduced value of the constant  $r_0$  as we move from the lightest O nuclei to the heaviest Pb isotopes. However, it is possible to provide a better description by choosing the radius constant to have isospin dependence. As noted above these predictions are found to be in good agreement with the available measurements for the neutron rms radii. We have, however, not shown the measured data to keep the figure uncluttered. Also, from fig. 33 it is seen that the best candidate for experimental observation of halo formation in the neutron rich nuclei is offered by the Ca isotopes. For the neutron rich heavy Zr isotopes this effect is less dramatic as is seen from fig. 33.

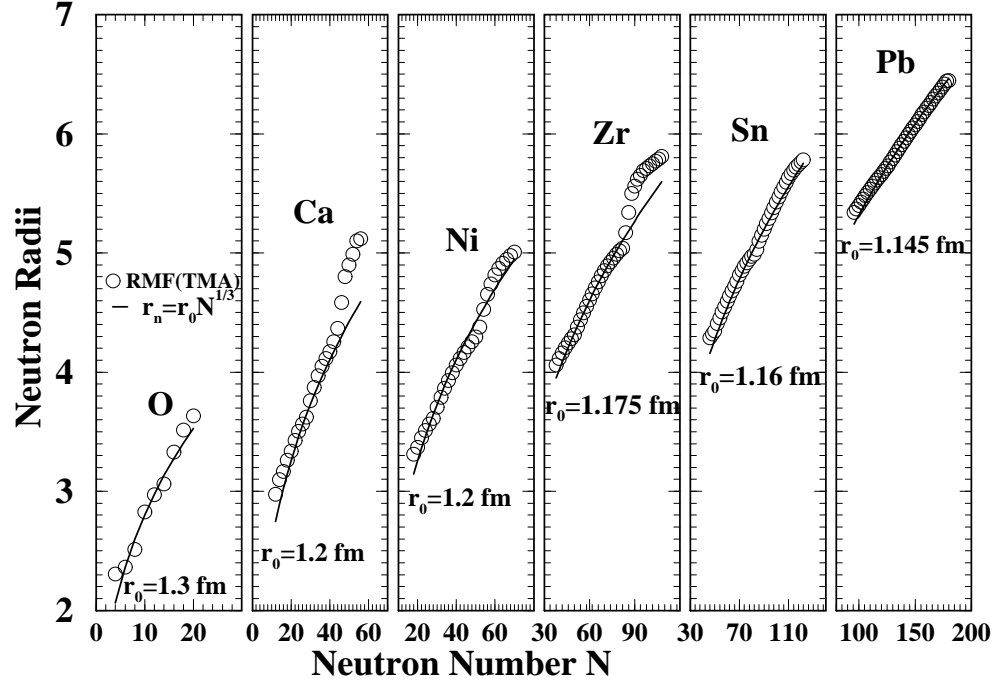


**Fig. 33.** The present RMF results for the neutron rms radii  $r_p$  for the isotopes of various nuclei obtained with the TMA force parameters. These results are compared with a rough estimate of neutron distribution radius given by  $r_n = r_0 N^{1/3}$  wherein the radius constant  $r_0$  is chosen to provide the best fit to the theoretical results. Halo formation in the case of neutron rich Ca and also to some extent in Zr isotopes is clearly seen.

### 3.3.4. Proton and Neutron Densities

We have already discussed the radial proton and neutron densities for  $^{66}\text{Ca}$  and  $^{84}\text{Ni}$  isotopes as representative examples of neutron rich Ca and Ni nuclei. Similar plots for the proton radial densities shown by hatched areas and neutron densities depicted by solid lines have been displayed in fig. 34 for selected neutron rich isotopes of  $^{20}\text{O}$ ,  $^{138}\text{Zr}$ ,  $^{170}\text{Sn}$  and  $^{250}\text{Pb}$  nuclei. In addition, the plots also depict the neutron densities of several other neighboring isotopes of these nuclei for the purpose of comparison. For completeness we have included the plots for the neutron rich  $^{62}\text{Ca}$  and  $^{96}\text{Ni}$  isotopes as well.



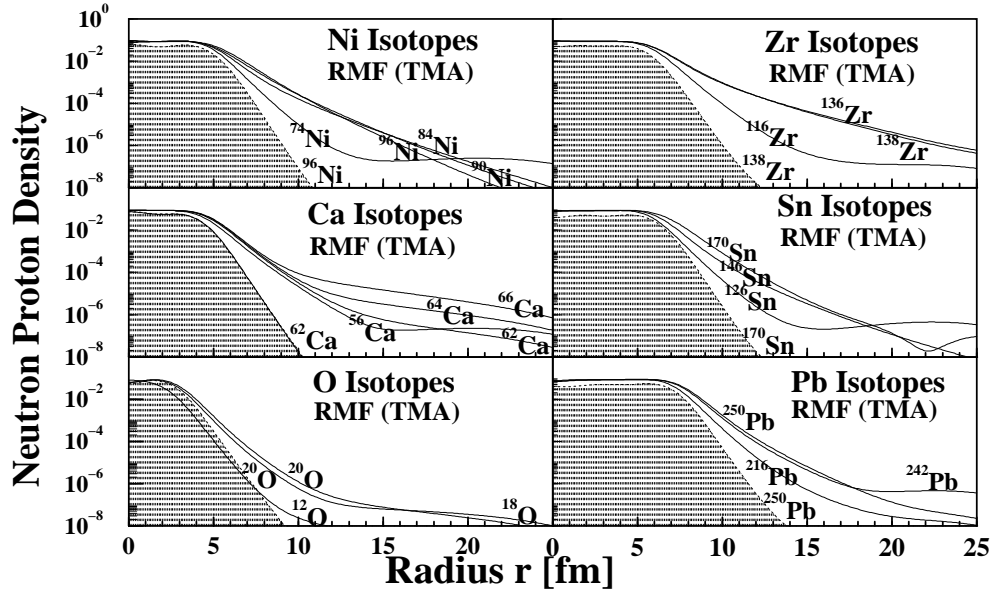


**Fig. 34.** The neutron radial density distributions for some selected isotopes of O, Ca, Ni, Zr, Sn and Pb nuclei have been shown by solid lines. The hatched area represents the proton radial density distribution for the nuclei  $^{20}\text{O}$ ,  $^{62}\text{Ca}$ ,  $^{96}\text{Ni}$ ,  $^{138}\text{Zr}$ ,  $^{172}\text{Sn}$  and  $^{250}\text{Pb}$ .

It is seen from fig. 34 that the proton densities for these nuclei have gross features similar to each other, albeit with increasing atomic number from O to Pb the distribution assumes wider spatial extension as expected. However, in the case of Zr isotopes, the distribution is relatively broader due to the fact that it is not a proton magic nucleus as compared to other nuclei shown in the figure. This can be easily seen from the difference in the slope of the density curves. As remarked earlier, for the open shell isotopes the asymptotic behavior of the density profile is affected by the contributions from the partially occupied positive energy resonant states and those loosely bound ones just above the continuum threshold near the Fermi level. The positive energy states have wide spread wave functions and yield a density profile with wide spatial extension and long tail asymptotically. This has been described earlier for the Ca and Ni isotopes and is found valid for other nuclei as well. Accordingly for further demonstration we have shown explicitly in figs. 35 through 40 the neutron and proton density profiles for the Zr, Sn and Pb isotopes. The inset in these plots shows the density distributions on a logarithmic scale for larger radial distances and exhibits its asymptotic behavior. In order to keep the plots uncluttered we have drawn the results for limited number of isotopes for a given chain.

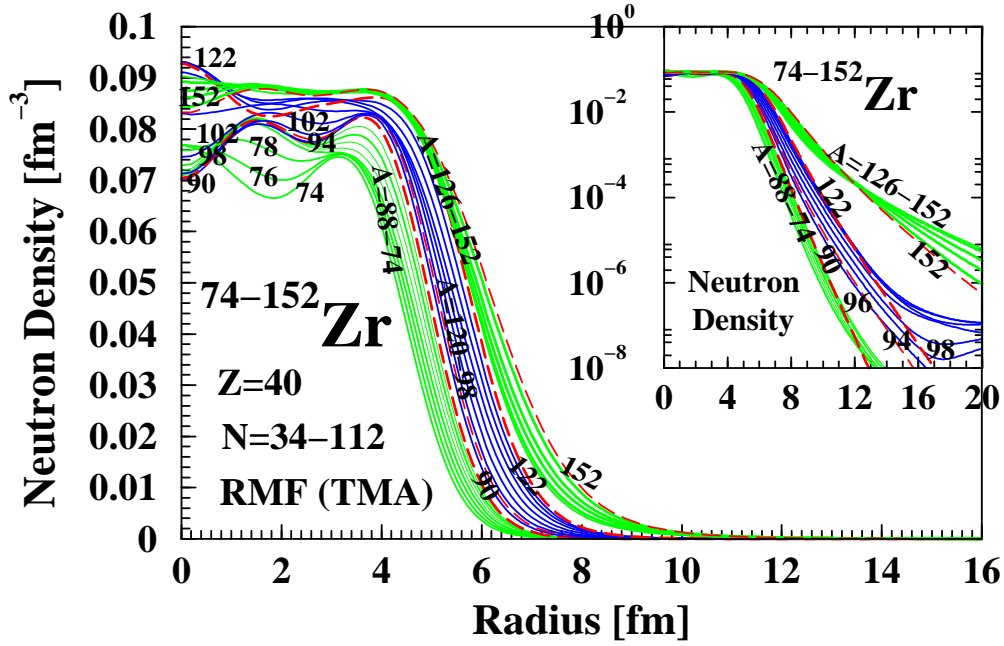
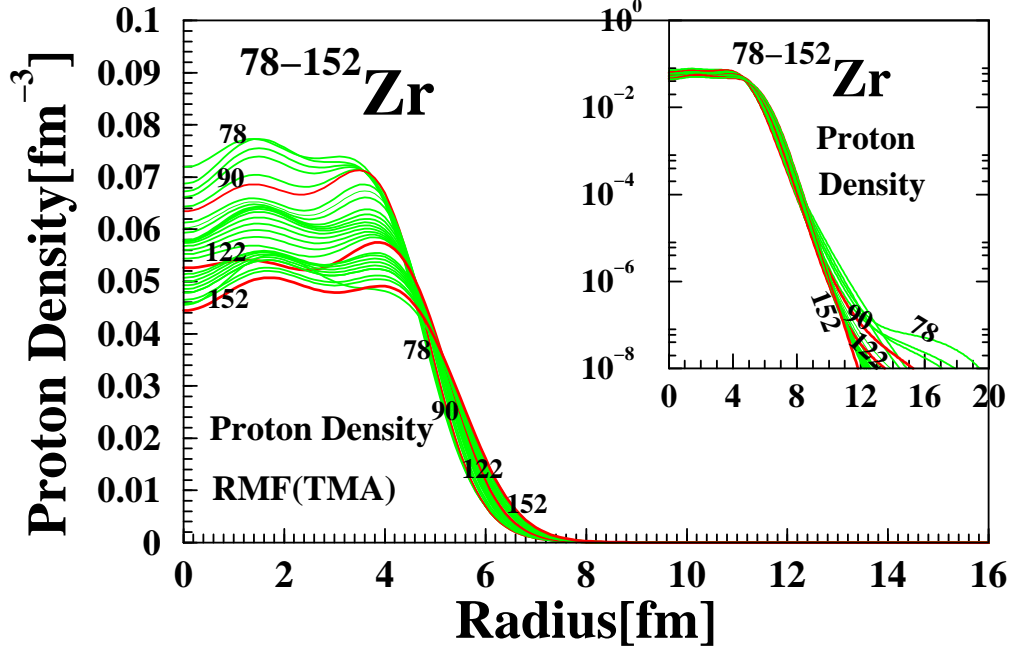


Fig. 35. The solid line show the neutron radial density distribution for the  $^{74-152}\text{Zr}$  isotopes obtained in the RMF+BCS calculations using the TMA force. To keep the figure uncluttered the distributions for only some selected isotopes covering the entire range have been plotted.

It is seen from the neutron densities of Zr isotopes in fig. 35 that for the neutron number  $N = 50, 82$  and  $112$  which correspond to shell closures in the  $^{90,122,152}\text{Zr}$  neutron rich nuclei, the density distribution is rather confined to smaller radial distances and diminishes quickly as is indicated by the slope of these curves shown in the inset. For other isotopes the distribution exhibits tendency to fall off sharply up to a radial distance of about 10 to 15 fm and then becomes flat. In the case of highly neutron rich isotopes  $N \geq 84$  corresponding to  $^{124-150}\text{Zr}$  the density profile has slightly altered feature in that it is characterized by a much slower fall as a function of radial distance and has wider spatial extension. This makes the curves for these isotopes to be well separated from the others as is seen from the inset in fig. 35. As explained earlier it is due to contributions from the positive energy states which are partially occupied, though with very small occupancy weights, and are either resonant or loosely bound states lying near the Fermi level. However, the density distributions tend to be similar to those found for the Ca isotopes.

Results for the proton density distributions for the chain of Zr isotopes have been depicted in fig. 36. The density distributions tend to show deviation from sharp fall off after about  $r = 10$  fm and is caused due to the fact that Zr not being a proton magic has contributions to the pairing correlations from the low lying resonant states. However, these deviations are unimportant as the magnitude of density for large distances has already diminished to the order of  $10^{-8} \text{ fm}^{-3}$ .

Further, fig. 36 shows that the central proton density decreases with increasing neutron number and may be attributed to the neutron-proton interaction. The maximum to minimum ratio of the central proton density value turns out to be higher than that for the corresponding central neutron densities. It is also seen from fig. 36 that with increasing neutron number the proton radius increases.



**Fig. 36.** The solid line show the proton radial density distribution for the  $^{74-152}\text{Zr}$  isotopes obtained in the RMF+BCS calculations using the TMA force. To keep the figure uncluttered the distributions for only some selected isotopes covering the entire range have been plotted.

In contrast to the Ca and Zr nuclei, the density profile of Sn isotopes is less extended and for heavier Sn isotopes it falls off rather rapidly as is seen from the inset in fig. 37. For smaller distances the density profile exhibits peak around  $r = 4 - 5$  fm. Between  $r = 5$  and 10 fm the density curves show identical radial dependence with a rapid smooth fall off. The distributions for isotopes with neutron number  $N = 100, 132$  and  $N = 176$  corresponding to neutron shell closures in the Sn isotopes are distinctly characterized by sharp fall off as can be seen in the inset of the figure. For these isotopes there are no contributions to the wave functions coming from resonant states in the continuum. For other isotopes one observes the flattening of the distribution at large distances indicating the contribution from the resonant and other positive energy states near the Fermi level.

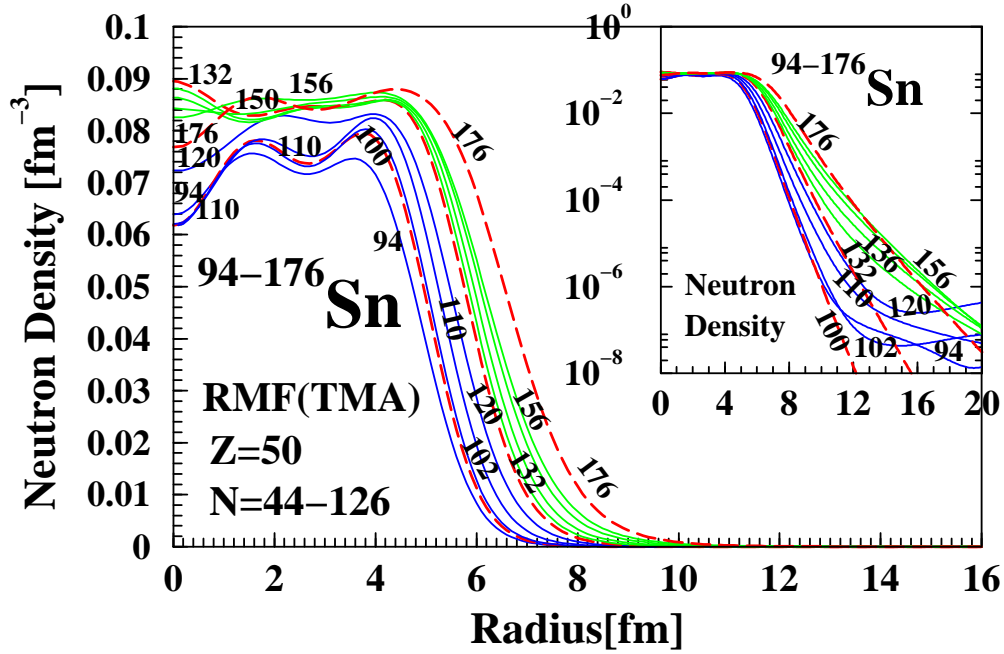
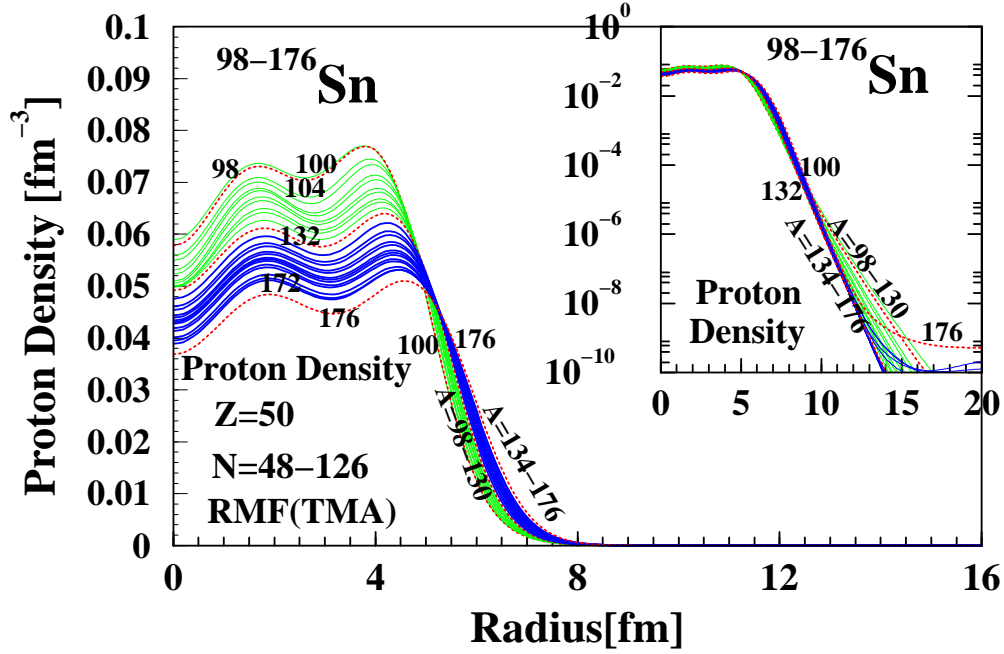


Fig. 37. The solid line show the neutron radial density distribution for some selected Sn isotopes obtained in the RMF+BCS calculations using the TMA force.

The proton density profile for the Sn isotopes depicted in fig. 38 shows spatially confined distributions. Again, with increasing neutron number the proton distribution radii are seen to grow. It is found that for heavy neutron rich Sn isotopes the proton single particle potential is changed and the Sn isotopes no longer have proton shell closure for  $Z = 50$ . For such isotopes then there are contributions from resonant states to the proton pairing correlations. Consequently for neutron rich isotopes the asymptotic proton density distributions becomes flat at the tail end as can be seen in the inset of fig. 38. The ratio of central maximum and minimum proton densities in this case has almost similar value ( $\approx 1.6$ ) as for the proton densities of Zr isotopes. The lightest isotope  $^{78}\text{Zr}$  is seen to have maximum proton density at the center whereas the minimum is that of heaviest isotope  $^{176}\text{Zr}$ . In contrast, the neutron density for the heaviest isotope is not maximum at the center as is evident from fig. 37.



**Fig. 38.** The solid line show the proton radial density distribution for some selected Sn isotopes obtained in the RMF+BCS calculations using the TMA force.

The neutron density profile of Pb isotopes plotted in fig. 39 shows much less spatial spread of the distributions. However, one clearly sees the slight flattening of the tails as depicted in the inset in fig. 39. In order to have some feeling of single particle states being filled in for we consider for example the isotope  $^{242}\text{Pb}$ . For this isotope the low lying neutron resonant state  $1j_{15/2}$  becomes bound and the positive energy  $1j_{13/2}$  state at  $\epsilon = 3.07$  MeV acts as resonant state. The occupancy weight of this state indicates that there are about 0.2 nucleons occupying this state in the continuum. This state contributes to the density at larger distances and, thus, the asymptotic density does not show a rapid fall off for such isotopes. Similar results are also obtained for other Pb isotopes. However, the isotopes  $^{208}\text{Pb}$  and  $^{266}\text{Pb}$  corresponding to  $N = 126$  and  $N = 184$  are neutron closed shell nuclei and for these two the spatial spread in the neutron density is seen to be minimum as is evident from the asymptotic density distribution shown in the inset of fig. 39. For smaller distances the density profile exhibits peak around  $r = 5.5$  fm. As in other cases the neutron density falls off quickly between  $r = 6$  and 10 fm.

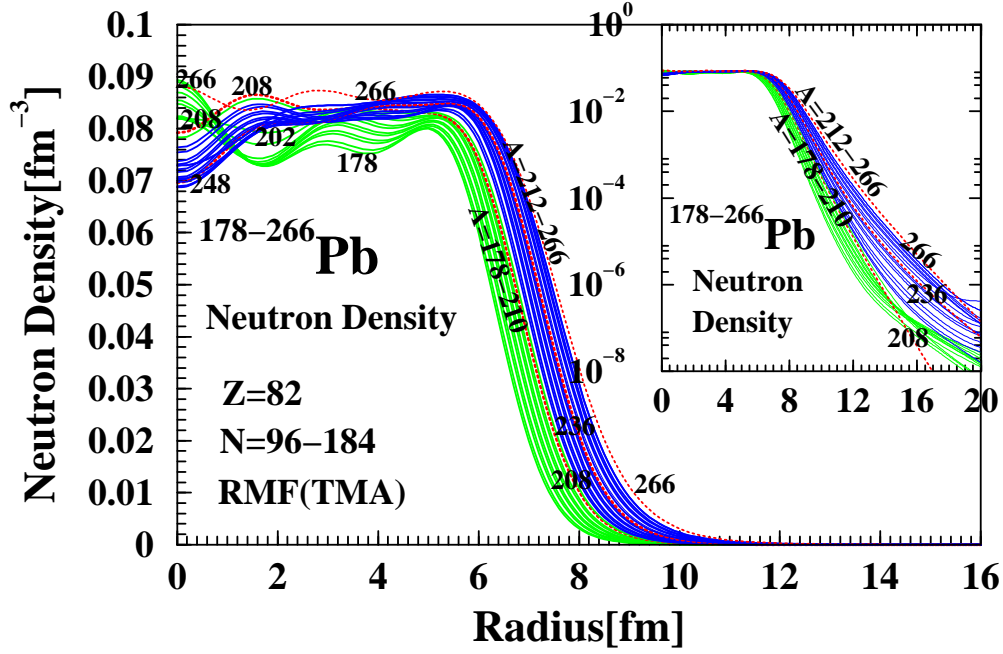


**Fig. 39.** The solid line show the neutron radial density distribution for some selected Pb isotopes obtained in the RMF+BCS calculations using the TMA force.

Similar to the neutron densities, and also as the Pb isotopes are proton magic, the proton densities of Pb isotopes have smaller spatial widening at the tail end as is seen in the inset of fig. 40. However, it is found, as for the other heavier isotopes of Sn, that in the case of heavy neutron rich Pb isotopes the single particle potential for the protons become much deeper and proton single particle energies are slightly changed and  $Z = 82$  no more corresponds to a proton shell closure. Due to contributions from proton positive energy states this is found to change the asymptotic proton density for the neutron rich Pb isotopes as can be seen in the inset of fig. 40. For small radial distances ( $r < 1$  fm), in contrast to Zr and Sn proton densities, here one observes an upward growth of the proton density near the center for the lighter isotopes ( $A = 178 - 208$ ). However, the neutron densities are in general larger than the proton densities. At the surface the proton densities have values between  $0.05$  and  $0.07 \text{ fm}^{-3}$  whereas the neutron densities for the Pb isotopes at the surface range between  $0.08$  and  $0.088 \text{ fm}^{-3}$ .

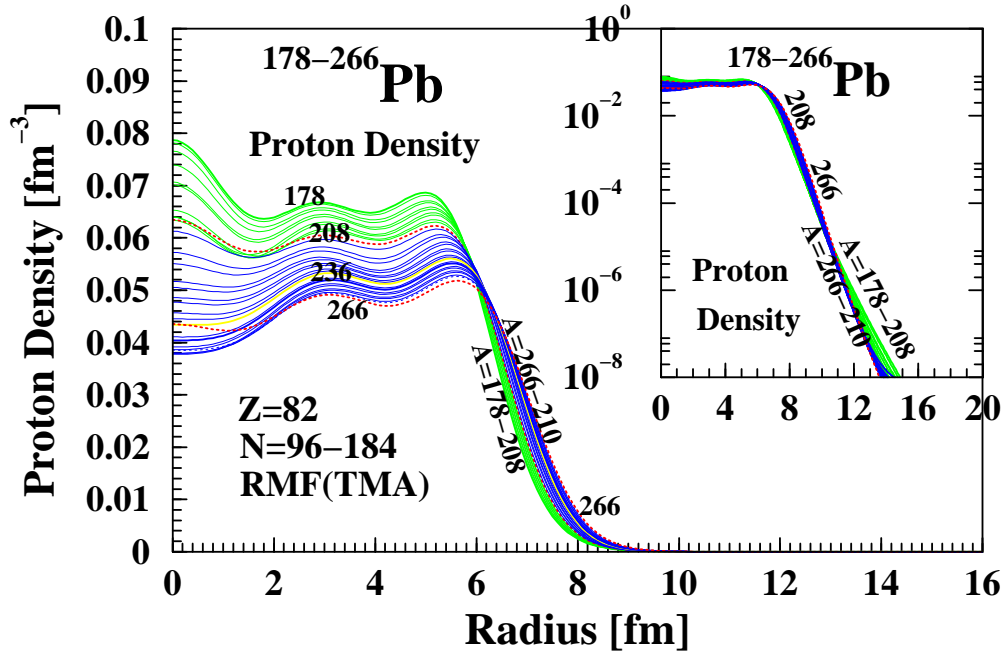


Fig. 40. The solid line show the proton radial density distribution for some selected Pb isotopes obtained in the RMF+BCS calculations using the TMA force.

#### 4. Summary

In the present investigation we have carried out a detailed study of the chains of isotopes of proton magic nuclei O, Ca, Ni, Sn and Pb, as well as that of Zr considered to be proton sub-magic within the framework of RMF+BCS. Our present calculations have been restricted to spherical shapes for the sake of simplicity. However, guided by our experience, we believe that calculations with the inclusion of deformation would not change the main conclusions reached for the proton magic nuclei investigated here.

In view of the fact that the pairing correlations play an important role for the description of neutron rich isotopes, we have also studied in detail the pairing properties of these nuclei close to the neutron drip line within the RMF+BCS framework. In the BCS calculations we have replaced the continuum by a set of positive energy states determined by enclosing the nucleus in a spherical box. It is found that from amongst the positive energy states, apart from the single particle states adjacent to the Fermi level, the dominant contribution to the pairing correlations is provided by a few states which correspond to low-lying resonances. As the number of neutrons increases the low lying resonant states become bound and the higher ones become more crucial for the description of pairing correlations. The loosely bound single particle states lying at the continuum threshold near the Fermi level are found to be important especially for the neutron rich isotopes. For the case

of O, Ca, Ni, Zr, Sn and Pb isotopes we have shown that the RMF+BCS and the RHB calculations<sup>19</sup> as well as other mean-field descriptions<sup>2-7</sup>, give similar results for the two-neutron separation energies, and for the proton, neutron and matter rms radii up to the neutron drip line. Further, it is found that these results are in good agreement with the available experimental data.

For the the case of Ca and Ni isotopes, and to some extent for the Zr nuclei, we have discussed the results in greater details. These RMF+BCS calculations have been explicitly shown to agree very well with the recent continuum relativistic Hartree-Bogoliubov (RCHB) calculations<sup>26</sup>. Moreover, the results obtained from two different popular RMF parameterizations, the TMA and the NL-SH forces, are also shown to be very similar to each other and with those of the RCHB. Small differences between the results for the two forces are traced back to the differences in the single particle spectrum near the Fermi surface. The difference is seen to be more pronounced for the neutron rich Zr isotopes which are not exactly proton magic. Further, this difference in the single particle structure leads to difference in the prediction of the two-neutron drip line for the TMA and NL-SH forces for the Zr isotopes. However since the binding energy difference amongst the neutron rich two isotopes of Zr is found to be less than 100 keV this difference should not be taken too seriously. The results for the Ca isotopes showing a sudden increase in the radii of neutron distribution for the neutron rich isotopes with  $N \geq 42$  provide evidence for a halo formation in the  $^{62-72}\text{Ca}$  isotopes. For halo formation in the neutron rich  $^{62-72}\text{Ca}$  isotopes the neutron  $3s_{1/2}$  state turns out to be the most crucial one. Calculations for the Zr isotopes yield similar results with indications, though less pronounced, for the halo formation in the neutron rich (Zr) isotopes. In this case the neutron  $3p_{1/2}$  state in the neutron rich Zr isotopes is found to play the key role. The results for the neutron rich isotopes of other nuclei, O, Ni, Sn and Pb do not show such a tendency of abrupt growth in the radii of the neutron distribution.

Similar indications with regard to halo formations and other properties are also provided by the calculated neutron and proton density profiles for these nuclei. The neutron density distributions for the isotopes with halo formation are seen to have a wide spatial extension. Further, it is found that the resonant states and the loosely bound states near the continuum threshold tend to accommodate a very small number of neutrons which in turn affect the radial dependence of the density profile at large distances. This contribution, though extremely small, makes the asymptotic density fall off less rapidly. However, for the neutron magic nuclei the distribution falls off sharply as it has no contributions from the resonant states. Similarly, the proton density distributions for the proton magic nuclei are found to be confined to smaller distances and fall off rapidly. However, for neutron rich proton magic nuclei the proton single particle potential becomes deeper and the shell closure property is destroyed. For such heavy neutron rich isotopes the asymptotic proton density is slightly affected by the contributions from the positive energy and resonant states. The Zr isotopes are not proton magic and thus in this case the proton density are found to have wider spatial extension and rather a slow fall off due to pairing correlations from positive energy states near the continuum threshold.

The detailed comparison of different results obtained from the RMF+BCS and



the Hartree-Bogoliubov frameworks on the one hand, and a reasonably good agreement of these with the available experimental data together confirm our earlier findings<sup>28</sup>, and provide ample indications that the RMF+BCS approach can be considered as a good approximation, in addition to being neat and transparent, to the full Relativistic Hartree-Bogoliubov (RHB) treatment for the drip-line neutron rich nuclei. This in fact is not surprising in view of similar conclusion reached very recently by Grasso *et al.*<sup>7</sup> for the non-relativistic mean field descriptions.

### Acknowledgments

We thank N. Sandulescu and G. Hillhouse for fruitful discussions. We are indebted to J. Meng for communicating some of his RCHB results before publication. One of the authors (HLY) gratefully acknowledges the support provided to him under the COE Professorship Program of Monbusho of the Osaka University, Japan, and the support through a grant by the Department of Science and Technology(DST), India. HLY would also like to thank Prof. Faessler for his kind hospitality while visiting Institut für Theoretische Physik der Universität Tübingen, Germany where part of this work was carried out.

### References

1. I. Tanihata, *J. Phys. G* **22**, 157 (1996); I. Tanihata *et al.*, *Phys. Rev. Lett.* **55**, 2676 (1985).
2. J. Dobaczewski, H. Flocard and J. Treiner, *Nucl. Phys. A* **422**, 103 (1984).
3. J. Terasaki, P.-H. Heenen, H. Flocard and P. Bonche, *Nucl. Phys. A* **600**, 371 (1996).
4. J. Dobaczewski, W. Nazarewicz, T. R. Werner, J. F. Berger, C. R. Chinn and J. Decharge, *Phys. Rev. C* **53**, 2809 (1996).
5. N. Sandulescu, R. J. Liotta and R. Wyss, *Phys. Lett. B* **394**, 6 (1997).
6. N. Sandulescu, Nguyen Van Giai and R. J. Liotta, *Phys. Rev. C* **61**, 061301(R) (2000).
7. M. Grasso, N. Sandulescu, Nguyen Van Giai and R. J. Liotta, *Phys. Rev. C* **64**, 064321 (2001).
8. J. D. Walecka, *Ann. Phys. (N.Y.)* **83**, 491 (1974).
9. B. D. Serot and J. D. Walecka, *Adv. Nucl. Phys.* **16**, 1 (1986).
10. P.-G. Reinhard, M. Rufa, J. Marhun, W. Greiner and J. Friedrich, *Z. Phys. A* **323**, 13 (1986).
11. A. Bouyssy, J.-F. Mathiot, Nguyen Van Giai, and S. Marcos, *Phys. Rev. C* **36**, 380 (1987).
12. P-G Reinhard, *Rep. Prog. Phys.* **52**, 439 (1989) and references therein.
13. Y. K. Gambhir, P. Ring and A. Thimet, *Ann. Phys. (N.Y.)* **198**, 132 (1990).
14. H. Toki, Y Sugahara, D. Hirata, B. V. Carlson and I. Tanihata, *Nucl. Phys. A* **524**, 633 (1991).
15. R. Brockman and H. Toki, *Phys. Rev. Lett.* **68**, 3408 (1992).
16. D. Hirata, H. Toki, I. Tanihata and P. Ring, *Phys. Lett. B* **314**, 168 (1993).
17. Y Sugahara and H. Toki, *Nucl. Phys. A* **579**, 557 (1994); Y Sugahara, Ph.D. Thesis, Tokyo Metropolitan University, 1995.
18. P. Ring, *Prog. Part. Nucl. Phys.* **37**, 193 (1996) and references therein.

19. J. Meng, *Phys. Rev. C* **57**, 1229 (1998).
20. G. A. Lalazissis, D. Vretenar and P. Ring, *Phys. Rev. C* **57**, 2294 (1998).
21. S. Mizutori, J. Dobaczewski, G. A. Lalazissis, W. Nazarewicz and P. G. Reinhard, *Phys. Rev. C* **61**, 044326 (2000).
22. M. Del Estal, M. Contelles, X. Vinas and S. K. Patra, *Phys. Rev. C* **63**, 044321 (2001).
23. A. M Lane, *Nuclear Theory* (Benjamin, 1964).
24. P. Ring and P. Schuck, *The Nuclear many-body Problem* (Springer, 1980).
25. G. Audi and A. H. Wapstra, *Nucl. Phys. A* **595**, 409 (1995).
26. J. Meng, H. Toki, J.Y. Zeng, S. Q. Zhang and S. Q. Zhou, *Phys. Rev. C* **65**, 041302(R) (2002).
27. M. M. Sharma, M. A. Nagarajan and P. Ring, *Phys. Lett. B* **312**, 377 (1993).
28. H. L. Yadav, S. Sugimoto and H. Toki, *Mod. Phys. Lett. A* **17**, 2523 (2002); Preprint, RCNP, Osaka University, Osaka (2001)
29. J. Meng and P. Ring, *Phys. Rev. Lett* **80**, 460 (1998).
30. J. Meng *Nucl. Phys.* **635**, 3 (1998).
31. J. Dechargé and D. Gogny *Phys. Rev. C* **21**, 1568 (1980).
32. J. Dobaczewski, W. Nazarewicz and T. R. Werner *Phys. Scr. T* **56**, 15 (1995).
33. H. de Vries, C. W. de Jager and C. de Vries, *At. Data Nucl. Data Tables* **36**, 495 (1987).
34. C. J. Batty, E. Friedman, H. J. Gils and H. Rebel, *Adv. Nucl. Phys.* **19**, 1 (1989).
35. M. Fauerbach et al. *Phys. Rev. C* **53**, 647 (1996); A. Ozawa et al. *Nucl. Phys. A* **673**, 411 (2000).
36. J. Leja and S. Gmuca, *Acta Phys. Slov.* **51**, 201 (2001).

Table 1: Parameters of the Lagrangian TMA and NL-SH together with the nuclear matter properties obtained with these effective forces.

<i>Param.</i>		<i>TMA</i>	<i>NL-SH</i>
M	(MeV)	938.9	939.0
$m_\sigma$	(MeV)	519.151	526.059
$m_\omega$	(MeV)	781.950	783.0
$m_\rho$	(MeV)	768.100	763.0
$g_\sigma$		$10.055 + 3.050/A^{0.4}$	10.444
$g_\omega$		$12.842 + 3.191/A^{0.4}$	12.945
$g_\rho$		$3.800 + 4.644/A^{0.4}$	4.383
$g_2$	(fm) <sup>-1</sup>	$-0.328 - 27.879/A^{0.4}$	-6.9099
$g_3$		$38.862 - 184.191/A^{0.4}$	-15.8337
$c_3$		$151.590 - 378.004/A^{0.4}$	
Nuclear Matter Properties			
saturation density $\rho_0$	(fm) <sup>-3</sup>	0.147	0.146
Bulk binding energy/nucleon (E/A) <sub>∞</sub>	(MeV)	16.0	16.346
Incompressibility K	(MeV)	318.0	355.36
Bulk symmetry energy/nucleon $a_{Sym}$	(MeV)	30.68	36.10
Effective mass ratio $m^*/m$		0.635	0.60